Energy 338 (2025) 138693

Contents lists available at ScienceDirect

Energy

journal homepage: www.elsevier.com/locate/energy

In-context learning for nano-PCM thermal behavior prediction in battery thermal management via Lattice Boltzmann simulation

Bichen Shang [b], Guo Li [c], Weijie Sun [d], Liwei Zhang [b], Guanzhe Cui [e], Jiyuan Tu [f], Xiang Fang [a,*], Xueren Li [f,g,**]

[a] School of Mechanical and Automotive Engineering, Shanghai University of Engineering Science, 201620, China
[b] School of Mechanical Engineering, Purdue University, West Lafayette, USA
[c] School of Low-carbon Energy and Power Engineering, China University of Mining and Technology, Xuzhou, 221116, China
[d] Department of Computing Science, University of Alberta, Edmonton, AB, T6G 2R3, Canada
[e] Department of Mechanical Engineering, The University of Melbourne, Melbourne, VIC, 3010, Australia
[f] School of Engineering, RMIT University, PO Box 71, Bundoora, VIC, 3083, Australia
[g] School of Safety Engineering, China University of Mining and Technology, Xuzhou, 221116, China

ARTICLE INFO

Handling editor: X Ou

Keywords:
Nano-PCM
Battery thermal management
Machine learning
TabPFN
Lattice Boltzmann method (LBM)

ABSTRACT

Effective thermal management is crucial for ensuring the safety and performance of lithium ion batteries in electric vehicles. While nano-enhanced phase change materials (nano-PCMs) offer excellent thermal regulation, their effectiveness is often limited by localized heat accumulation from natural convection. Existing ML-based studies mostly focus on temperature metrics alone, neglecting thermal uniformity and relying on black-box models with limited interpretability. This study proposed a zonal nanoparticle distribution strategy and utilized high-fidelity Lattice Boltzmann Method (LBM) simulations to investigate underlying heat transfer mechanisms in nano-enhanced PCM systems. The state-of-the-art Tabular Prior-data Fitted Network (TabPFN) was then employed to accurately predict key thermal indicators and was benchmarked against widely used models such as BPNNs, XGBoost, and CatBoost. Furthermore, SHapley Additive exPlanations (SHAP) analysis was applied to interpret TabPFN outputs, revealing key regional features and providing physical insights into system performance. The results demonstrated that with optimal non-uniform nanoparticle distribution pattern, the Nusselt number increased by 12.04 % and melting time was reduced by 13.05 %. TabPFN exhibited superior prediction accuracy compared to other popular machine learning models, with error bins generally lower in magnitude and reductions in MAE and RMSE by 8–92 % and 7–90 %. SHAP analysis further visualized quantitative correlation between training inputs and target variables and their influence on convective behavior and heat retention. The proposed explainable in-context learning framework based on TabPFN and SHAP is expected to provide valuable insights for guiding the design and optimization of advanced nano-PCM battery thermal management systems.

Nomenclature -

		Greeksymbols -	
c	Lattice speed [m·s^{-1}]	μ	Dynamic viscosity [kg·m^{-1} s^{-1}]
c_s	Lattice sound speed [m·s^{-1}]	ν	Kinetic viscosity [m^2·s^{-1}]
S	Volumetric force term	k	Thermal conductivity
θ	Local temperature	h	Enthalpy
t	Physical time	α	Thermal diffusivity

(*continued on next column*)

(*continued*)

C_p	Specific heat at constant pressure	ω_i	Weight coefficient in direction i
e_i	Discrete velocity in direction i [m·s−1]	ρ	Density [kg·m^{-3}]
F	Force [N] [kJ·kg^{-1} K^{-1}]	τ_f	Dimensionless relaxation time for density

(*continued on next page*)

* Corresponding author.
** Corresponding author. School of Engineering, RMIT Unversity, PO Box 71, Bundoora, VIC, 3083, Australia.
E-mail addresses: xiang.fang@sues.edu.cn (X. Fang), xueren.li@hotmail.com, xueren.li@rmit.edu.au (X. Li).

https://doi.org/10.1016/j.energy.2025.138693
Received 19 July 2025; Received in revised form 6 September 2025; Accepted 26 September 2025
Available online 4 October 2025

(*continued*)

F_i	Discrete force in direction i [kg·m^{-3} s^{-1}]	τ_g	Dimensionless relaxation time for enthalpy
f_i	Distribution function for density in direction i [kg·m^{-3}]	φ	Volume fraction
f_i^{eq}	Equilibrium distribution function for density in direction *i*	η	Sedimentation factor
f_i^{neq}	Non-equilibrium distribution function for density in direction *i*	***Subscripts***	
g	Acceleration due to gravity [m·s^{-2}]	*ave*	Average
g_i	Distribution function for total enthalpy in direction *i* [j·kg^{-1}]	*i*	Direction
g_i^{eq}	Equilibrium distribution function for total enthalpy in direction *i*	*s*	Solid
H	Total enthalpy [J·kg^{-1}]	*l*	liquid
h_{sl}	Latent heat [J·kg^{-1}]	*ref*	Reference
λ	Thermal conductivity [W·m^{-1} K^{-1}]	*melting*	Stage when PCM total melting
L	Characteristic length	***Abbreviation***	
Fo	Dimensionless time	*PCM*	Phase Change Materials
T^*	Dimensionless temperature	*LiBs*	Lithium-ion Batteries
ε	Temperature standard deviation	*BTMS*	Battery Thermal Management Systems
fl	Liquid fraction	*LBM*	Lattice Boltzmann Method
P_{cool}	Cooling power	*Ra*	Rayleigh number
CR	Mean cooling power ratio	*Pr*	Prandtl number
R^2	R-squared	*Ste*	Stefan number
MAE	Mean Absolute Error	*Nu*	Nusselt number
RMSE	Root Mean Squared Error	*BPNN*	Back Propagation Neural Networks
SHAP	Shapley Additive exPlanations	*XGBoost*	eXtreme Gradient Boosting
r	Radius	*CATBoost*	Categorical Boosting
–	–	*TabPFN*	Tabular Prior-data Fitted Network

1. Introduction

Rising global transport demand has driven greenhouse-gas emissions to record levels and strained fossil-fuel reserves [1], which spurs the shift toward battery electric vehicles (BEVs) as a scalable low-carbon alternative [2]. Lithium-ion powered EVs benefit from high energy density, fast charge–discharge capability, and long cycle life, yet face critical challenges as intense cycling generates substantial heat and uneven temperature profiles, which accelerate capacity loss and heighten the risk of thermal runaway [3,4]. Effective thermal management is therefore critical to preserve battery performance and safety, which spurs the development of accurate tools to assist in the design and optimization of Battery Thermal Management Systems (BTMS).

Existing BTMS are generally categorized as active, passive, or hybrid [5]. Active cooling (air, liquid) offers continuous heat removal but requires complex equipment, extra energy, and is mostly applied at module/pack scale [6–8]. PCM-assisted passive or hybrid cooling leverages latent heat for effective regulation and is applicable from cell to module level [9,10]. Significant progress has been achieved in PCM-based BTMS, including improvements in PCM properties [11], system configurations [12] and battery operational conditions [13]. However, several limitations remain, including the intrinsically low thermal conductivity of PCMs, safety concerns such as possible deformation and material flammability [14], and the tendency of melted PCM to migrate upward during operation, which can cause heat accumulation and non-uniform cooling [15].

To tackle the above challenges, strategies such as fins [16], thermal bridges [17], optimized layouts [18–20], refined enclosure geometries [18,19], and the incorporation of nanoparticle additives [21] have been proposed. Among these, dispersing conductive nanoparticles into PCM not only enhances thermal conductivity, but also mitigates migration-induced non-uniform cooling and contributes to improved structural and thermal stability. Research has tested a wide range of conductive fillers, including metals (Cu [22], Al [23,24]), metal oxides (Al2O3 [25,26], TiO2 [27], CuO [28]), and carbon-based materials (graphite [29], graphene [30], CNTs [31]). These fillers vary in shape (spherical, flake, tubular) [32,33], size (tens to hundreds of nanometers) [34], and volume fraction (typically 1–10 %) [35,36]. Nevertheless, while most studies emphasize homogeneous filler dispersion to improve bulk performance, whereas the issue of melted PCM migration and the consequent heat accumulation [15] still appears insufficiently addressed.

Beyond advances and limitations in system design, it is equally important to consider the research methodologies employed in BTMS studies. Current thermal management research mainly relies on experimental testing and numerical simulation [37,38]. While experiments provide precise real-world insights, they are costly, time-consuming, and limited in design coverage. CFD simulations offer high-fidelity results but require substantial computational resources and become impractical for large parameter spaces. Moreover, challenges such as PCM's limited thermal response under fast charging and trade-offs in cost, energy density, and integration highlight the need for a systems engineering perspective [39]. The high dimensionality of design variables, multi-material interactions, and diverse operating scenarios thus render traditional methods inadequate for rapid assessment and optimization. Hence, efficient and scalable data-driven approaches are urgently needed to accelerate BTMS development.

Machine learning (ML) has been increasingly applied to PCM thermal performance, showing promise in improving heat storage and transfer [40]. Common methods include Ar tificial Neural Networks (ANN) [41], Convolutional Neural Networks (CNN) [42], ensemble trees [43], Extreme Gradient Boosting (XGBoost) [44], Random Forests [45], and support vector machines (SVM) [46], which have been used to predict heat transfer parameters (e.g., Nusselt number) [47], temperature responses (surface and peak temperatures) [42,48], and energy metrics (liquid fraction [49], melt duration [50,51], heat storage capacity [52]) across different PCM compositions and conditions. However, most studies focus on thermal storage tanks and energy systems, with relatively few on PCM-BTMS. Notable efforts include Gu et al. [42], who developed a BKA-CNN-Self Attention model for a hybrid air-PCM BTMS (max. error 0.45 °C); Hasan et al. [49], who combined fins, metal foam, and PCM with ANN prediction (R2 = 0.98–0.99); Zhang et al. [53], who linked thermophysical properties of 50 PCMs to performance via CFD and BPNN-TOPSIS; and Xie et al. [54], who studied PCM–liquid hybrid cooling (up to 27.5 °C reduction) with Random Forest predictions (<5 % error). Despite progress, ML studies on PCM-BTMS face three limitations: (1) overemphasis on macroscopic averages with little attention to local heat accumulation from PCM convection; (2) limited focus on nano-PCM cooling scenarios; and (3) reliance on black-box models with poor interpretability. A unified, explainable ML framework is therefore needed for nanoparticle-enhanced PCM-BTMS.

Driven by the need to enhance battery safety and efficiency, PCM-BTMS have made progress. Yet, limited attention has been given to nanoparticle spatial distribution and temperature uniformity in nano-PCM systems, while data-driven methods with physical interpretability remain scarce. To address these aforementioned gaps, this study introduces a novel predictive framework utilizing recent advances in machine learning for PCM-BTMS applications. This study first proposes a zonal nanoparticle distribution strategy and employs the Lattice Boltzmann Method (LBM) to investigate the underlying heat transfer mechanisms in nano-enhanced PCM systems. One of the latest algorithms for tabular data, namely TabPFN (Tabular Prior-data Fitted Network), is employed to predict the thermal performance of nano-enhanced PCM systems and is benchmarked against several popular and widely used models, including Backpropagation Neural Networks

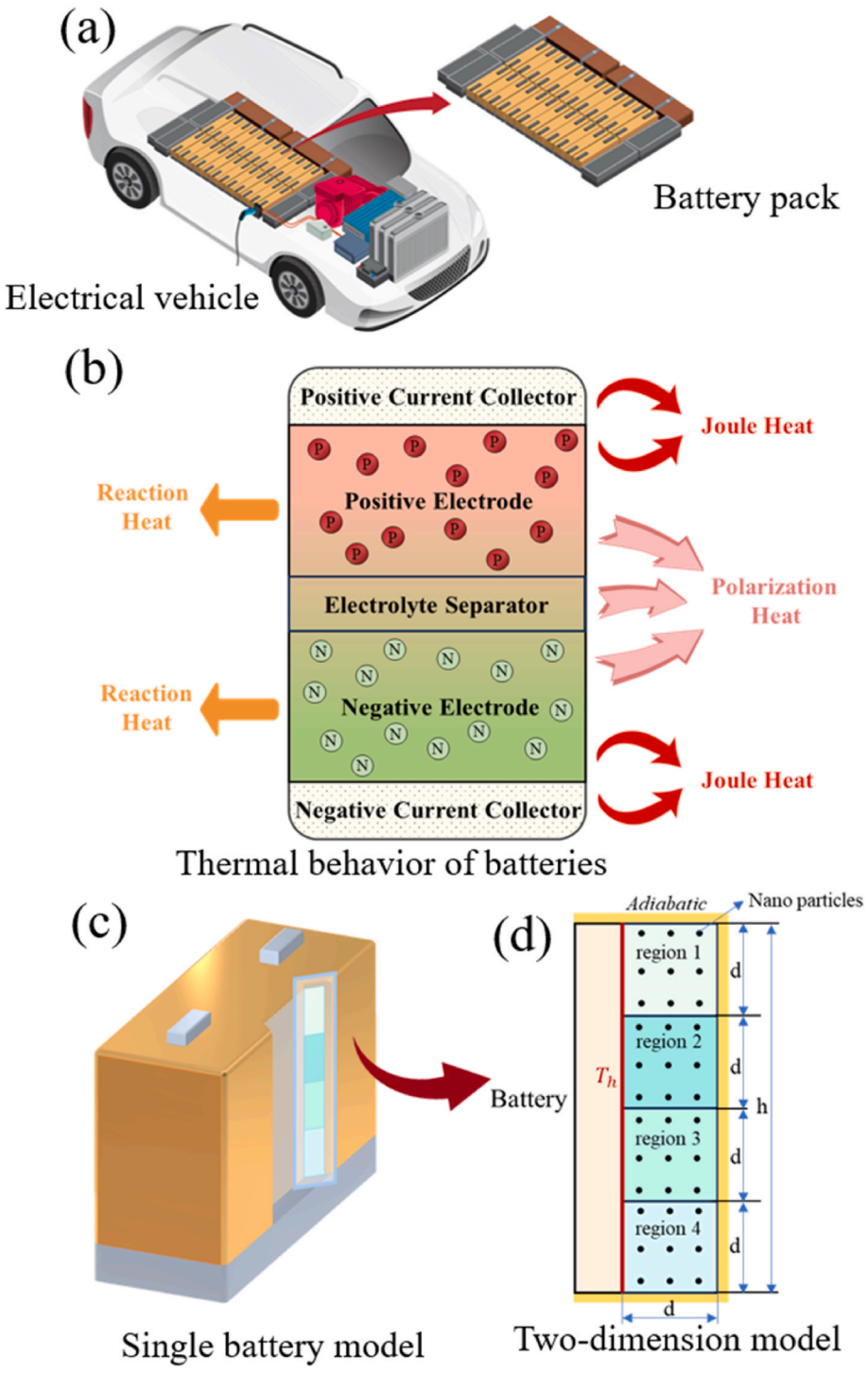

Fig. 1. The schematic of the battery thermal management system: (a) Electric vehicle; (b) Thermal behavior of batteries; (c) Single battery model; (e) Two dimensional model.

(BPNNs), Extreme Gradient Boosting (XGBoost), and CatBoost. SHAP (SHapley Additive exPlanations) analysis was further applied to interpret the model outputs and identify the key factors governing BTMS performance. This study is expected to offer a powerful and explainable predictive tool to guide the design and optimization of advanced PCM-BTMS.

2. Methodology

2.1. LBM simulation for nano-PCM based BTMS

2.1.1. Model description

In EV power systems, battery modules are composed of closely packed cylindrical cells, and multiple modules are assembled into a pack. The BTMS typically enables active thermal management at the module or pack level. However, heat dissipation between individual cells remains challenging due to the compact arrangement. In this work,

PCM is applied to encapsulate each cylindrical cell to achieve passive, cell-level thermal regulation, as illustrated in Fig. 1. The height of the battery is denoted as h, and the thickness of the surrounding annular PCM layer is d.

To prevent thermal accumulation in the upper region caused by PCM flow after melting, three partitions are introduced to divide the PCM into four equal sections. In addition, an average volume fraction of 5% Al2O3 nanoparticles is added into the PCM to enhance its thermal conductivity. The left boundary of the PCM is in contact with a heating wall maintained at a constant temperature T_h, while the other three boundaries are adiabatic.

This study focuses on the latent heat dissipation characteristics of the PCM during phase change and the effect of nanoparticle distribution. Therefore, the computational domain encompasses the annular PCM layer around the battery, while the internal electrochemical reactions are neglected.

2.1.2. Lattice Boltzmann method

In this investigation, PCM is modeled as a Newtonian, incompressible fluid exhibiting laminar flow behavior. The conservation laws governing mass, linear momentum, and thermal energy are formulated as follows [55]:

$$\frac{\partial \rho}{\partial t} + \nabla\cdot(\rho \boldsymbol{v}) = 0 \tag{1}$$

$$\frac{\partial(\rho \boldsymbol{v})}{\partial t} + \nabla\cdot(\rho \boldsymbol{v}\boldsymbol{v}) = -\nabla\pi + \nabla\cdot(\eta\nabla \boldsymbol{v}) + S \tag{2}$$

$$\frac{\partial(\rho c_p \theta)}{\partial t} + \nabla\cdot(\rho c_p \theta \boldsymbol{v}) = \nabla\cdot(\kappa\nabla\theta) + \dot{q} \tag{3}$$

where ρ, μ, k, C_p are the density, the dynamic viscosity, thermal conductivity and specific heat of PCM at constant pressure, respectively. p is the pressure, $\boldsymbol{u}$ is the velocity, T is tempreature.

The volumetric force term S and the heat source $\dot{q}$ due to latent heat exchange are expressed as:

$$\boldsymbol{S} = \rho \boldsymbol{g}\alpha_T(\theta - \theta_0) \tag{4}$$

$$\dot{q} = -\frac{\partial}{\partial t}(\rho\Delta h) - \nabla\cdot(\rho \boldsymbol{v}\Delta h) \tag{5}$$

The local temperature θ is related to the enthalpy h by the piecewise definition:

$$\theta = \begin{cases} \theta_s - \dfrac{h_s - h}{c_p}, h \le h_s \\ \theta_s + \dfrac{h - h_s}{h_l - h_s}, \quad h_s < h < h_l \\ \theta_l + \dfrac{h - h_l}{c_p}, h \ge h_l \end{cases} \tag{6}$$

To simulate the coupled fluid-thermal transport with phase transition, an enthalpy-based Lattice Boltzmann Method (LBM) is employed. The discrete evolution of distribution functions for mass and enthalpy, under the single-relaxation-time Bhatnagar–Gross–Krook (BGK) approximation, is formulated as [56,57]:

$$f_i(\boldsymbol{x} + \boldsymbol{c}_i\delta t, t + \delta t) = f_i(\boldsymbol{x}, t) - \frac{1}{\tau_\nu}\left(f_i - f_i^{eq}\right) + \delta t\Phi_i \tag{7}$$

Table 1
Thermal properties of nanoparticle and base PCM.

Material	ρ(kg /m^3)	C_p(J /kgK)	λ(W /mK)	μ(kg /ms)	h_{si}(J /kg)
Al_2O_3	3880	765	25.0	–	–
Paraffin	930	1600	0.21	9.2×10^{-4}	195000

$$h_i(\boldsymbol{x} + \boldsymbol{c}_i\delta t, t + \delta t) = h_i(\boldsymbol{x}, t) - \frac{1}{\tau_a}\left(h_i - h_f^{eq}\right) \tag{8}$$

The equilibrium distribution functions are given by:

$$f_i^{eq} = \omega_i\rho\left[1 + \frac{\boldsymbol{c_i}\cdot\boldsymbol{\nu}}{c_s^2} + \frac{(\boldsymbol{c_i}\cdot\boldsymbol{\nu})^2}{2c_s^4} - \frac{\boldsymbol{\nu}^2}{2c_s^2}\right] \tag{9}$$

$$h_i^{eq} = \omega_i\left[h + c_p\theta\left(\frac{\boldsymbol{c_i}\cdot\boldsymbol{\nu}}{c_s^2} + \frac{(\boldsymbol{c_i}\cdot\boldsymbol{\nu})^2}{2c_s^4} - \frac{\boldsymbol{\nu}^2}{2c_s^2}\right)\right] + \xi_i(c_p\theta - h) \tag{10}$$

For the D2Q9 velocity model, the weights ω_i and auxiliary coefficients ξ_i are:

$$\omega_i = \begin{cases} \dfrac{4}{9}, i = 0 \\ \dfrac{1}{9}, i = 1 \sim 4 \\ \dfrac{1}{36}, i = 5 \sim 8 \end{cases} \tag{11}$$

$$\xi_i = \begin{cases} -\sum_{j=1}^{8}\omega_j, i = 0 \\ \omega_i, i \ne 0 \end{cases} \tag{12}$$

$$\boldsymbol{c}_i = \begin{cases} (0,0), i = 0 \\ c(cos[(i-1)\pi/2]), sin[(i-1)\pi/2], i = 1 \sim 4 \\ \sqrt{2}c(cos[(2i-1)\pi/4]), (sin[(2i-1)\pi/4]), i = 5 \sim 8 \end{cases} \tag{13}$$

The forcing term Φ_i incorporating buoyancy is:

$$\Phi_i = \omega_i\left(1 - \frac{1}{2\tau_\nu}\right)\left(\frac{c_i - \nu}{c_s^2} + \frac{(c_i\cdot\nu)c_i}{c_s^4}\right)\cdot\rho b \tag{14}$$

$$\boldsymbol{b} = \boldsymbol{g}\alpha_T(\theta - \theta_\gamma) \tag{15}$$

The macroscopic physical fields are recovered as:

$$\rho = \sum_i f_i, \rho\boldsymbol{\nu} = \sum_i \boldsymbol{c}_i f_i + \frac{\delta t}{2}\rho\boldsymbol{b}, \boldsymbol{h} = \sum_i h_i \tag{16}$$

The kinematic viscosity ν and thermal diffusivity α are related to relaxation times via:

$$\nu = \left(\tau_\nu - \frac{1}{2}\right)\delta t c_s^2, \alpha = \left(\tau_\alpha - \frac{1}{2}\right)\delta t c_s^2 \tag{17}$$

$$\tau_\nu = \frac{\eta}{\rho c_s^2\delta t} + 0.5, \tau_\alpha = \frac{\kappa}{\rho c_p c_s^2\delta t} + 0.5 \tag{18}$$

The dimensionless time are given as:

$$Fo = \frac{\alpha t}{L^2} \tag{19}$$

2.1.3. Numerical setup

This study investigates latent heat dissipation during the phase change of PCM under various nanoparticle distribution strategies. Accordingly, the computational domain is confined to the annular PCM layer, with internal electrochemical processes omitted. Dirichlet boundary conditions are applied: initially ($Fo = 0$), the system is isothermal at T_0; as the simulation proceeds ($Fo > 0$), the heated wall is maintained at a constant temperature T_h.

The computation continues until thermal equilibrium is reached and the PCM has fully transitioned to the liquid phase. The governing equations are reformulated in a dimensionless framework using characteristic nondimensional variables. In this study, the Rayleigh number (Ra), Prandtl number (Pr), and Stefan number (Ste) are set to 5×10^4, 1, and 7, respectively. An in-house C++ solver based on the enthalpy-

Table 2
Representative distributions of Al_2O_3 nanoparticle volume fraction.

$$\begin{cases} \varphi_1+\varphi_2+\varphi_3+\varphi_4=0.200 \\ 0.035\le\varphi_1,\varphi_2,\varphi_3\le 0.065 \\ 0.050\le\varphi_4\le 0.095 \end{cases} \quad (26)$$

Type	Region 1	Region 2	Region 3	Region 4
Type 0	5.0 %	5.0 %	5.0 %	5.0 %
Type 1	5.5 %	4.5 %	5.5 %	4.5 %
Type 2	4.5 %	5.5 %	5.5 %	4.5 %
Type 3	6.0 %	4.0 %	4.0 %	6.0 %
Type 4	4.0 %	6.0 %	6.0 %	4.0 %
Type 5	6.5 %	3.5 %	3.5 %	6.5 %
Type 6	3.5 %	6.5 %	6.5 %	3.5 %

based lattice Boltzmann method is employed for the simulations.

Paraffin serves as the primary PCM, with aluminum oxide (Al_2O_3) introduced as a nanoparticle additive owing to its superior thermal conductivity and chemical stability [58]. The key thermophysical parameters of both substances are provided in Table 1.

The effective thermophysical properties of the nano-PCM are calculated as functions of the nanoparticle volume fraction φ, using the following empirical correlations:

$$\rho_{pcm}=(1-\varphi)\rho_{paraffin}+\varphi\rho_{Al_2O_3} \quad (20)$$

$$(\rho C_p)_{pcm}=(1-\varphi)(\rho C_p)_{paraffin}+\varphi(\rho C_p)_{Al_2O_3} \quad (21)$$

$$\lambda_{pcm}=\frac{\lambda_{Al_2O_3}+2\lambda_{paraffin}+2(\lambda_{Al_2O_3}-\lambda_{paraffin})\varphi}{\lambda_{Al_2O_3}+2\lambda_{paraffin}-(\lambda_{Al_2O_3}-\lambda_{paraffin})\varphi}\lambda_{paraffin} \quad (22)$$

$$\mu_{pcm}=0.983\mu_{paraffin}\,exp\,(12.959\varphi) \quad (23)$$

$$(\rho\beta)_{pcm}=(1-\varphi)(\rho\beta)_{paraffin} \quad (24)$$

$$(\rho h_{sl})_{pcm}=(1-\varphi)(\rho h_{sl})_{paraffin} \quad (25)$$

To assess the impact of nanoparticle distribution, a baseline case with uniformly dispersed nanoparticles at a volume fraction of 5.0% was first simulated. Building upon this, several representative non-uniform configurations summarized in Table 2were constructed. Finally, 343 distribution patterns were comprehensively evaluated. As defined in Equation (26), the nanoparticle volume fractions are constrained to maintain an average of 5.0%. The local values φ_i (i = 1 to 4) vary between 3.5% and 6.5% with a step size of 0.5%. This dataset forms a solid foundation for subsequent machine learning applications [59–61].

2.1.4. PCM-BTMS model validation

The modeling approach was verified through a two-stage validation process. In the first step, the accuracy of the LBM method for heat conduction was assessed using a benchmark case of a two-dimensional square cavity filled with PCM initially at its melting temperature T_m. The left boundary was maintained at a constant temperature T_h, where $T_h > T_m$, to initiate melting. Fig. 2(a) and 2(b) presents a comparison of the predicted average Nusselt number ($N\bar{u}_{ave}$) and liquid fraction (fl) from the present model against the analytical solu-tion reported by

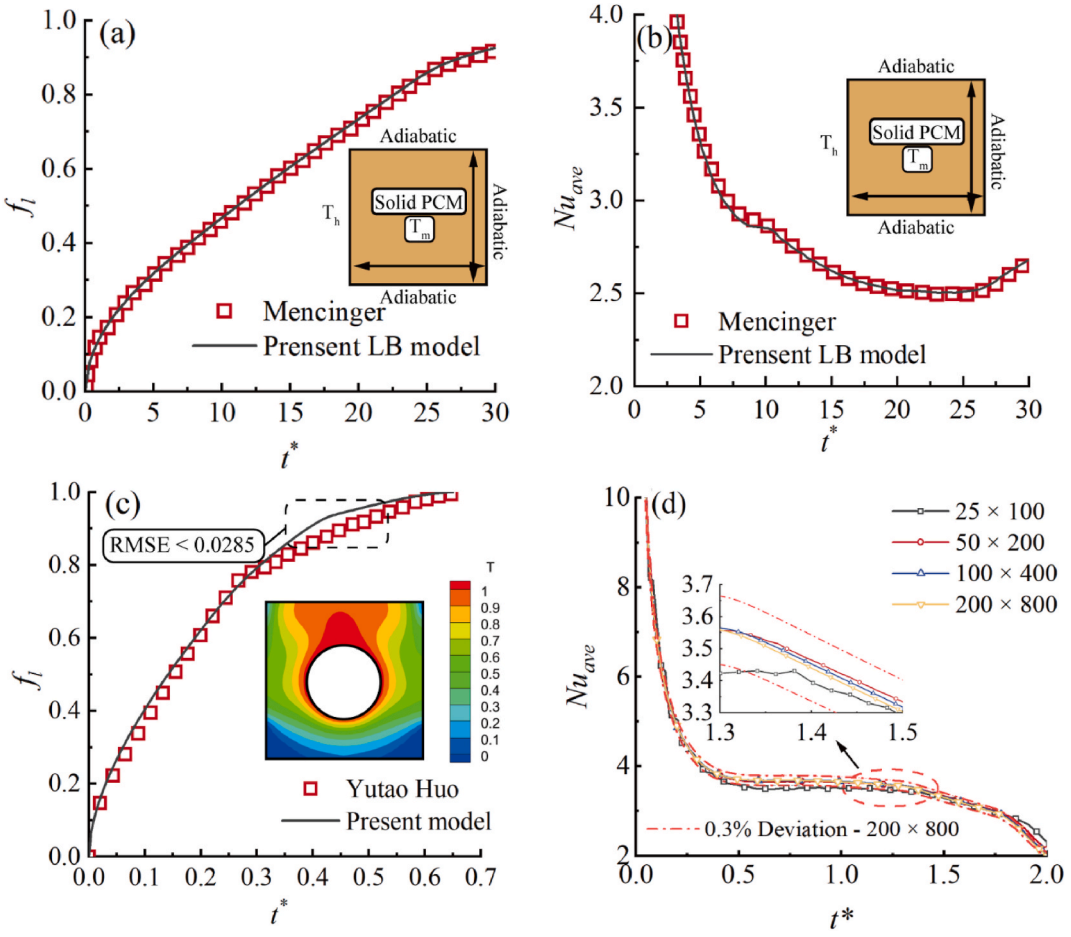

Fig. 2. (a) Validation on liquid fraction (fl); (b) Validation on Nusselt number (Nu_{avg}); (c) Validation of PCM-BTMS model compared to Huo et al.'s study; (d) Mesh independence test.

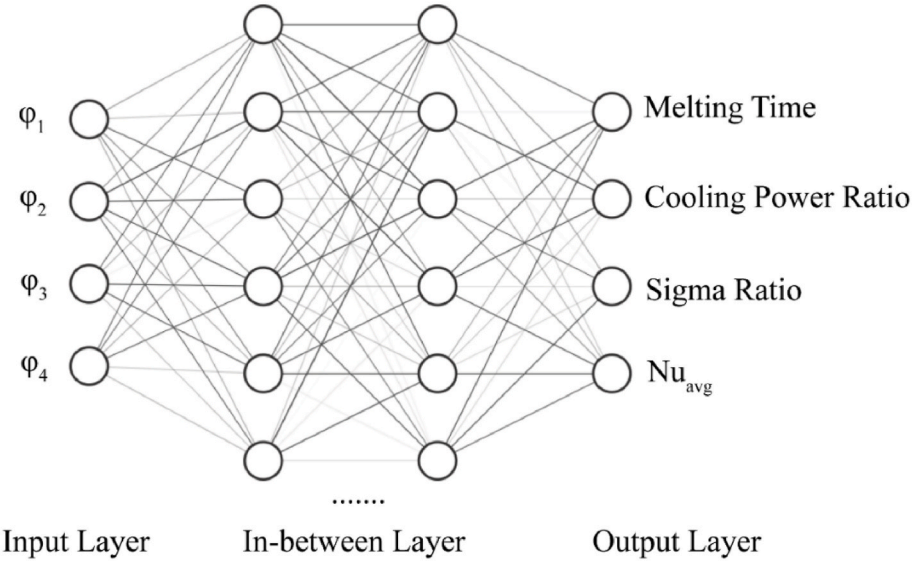

Fig. 3. Schematic diagram of BPNN architecture (training feature φ is the concentration of nanoparticles in region 1, 2, 3 and 4), please see Fig. 1(d).

Mencinger [62]. The results show that discrepancies remained within 2%, demonstrating the reliability of the proposed numerical approach.

The second stage of validation involved assessing the PCM-based BTMS performance by comparison with a published numerical benchmark. Specifically, the reference case considered a cylindrical battery embedded at the center of a square PCM block, as described in Huo's study [63]. The battery has a radius r, and the surrounding PCM module is a square with side length L, with a radius-to-length ratio of $r/L = 0.22$. Fig. 2(c) shows the comparison of the predicted liquid fraction between the present LBM results and those reported in the reference. The overall RMSE was found smaller than 0.0285, confirming the robustness and fidelity of the developed model in capturing phase-change behavior in PCM–battery systems. Moreover, the LBM approach adopted in this study for PCM anal ysis has also been widely applied in previous works [51,64], which collectively attest to the reliability of this method.

To enhance computational efficiency while maintaining accuracy, a grid independence study was conducted. Fig. 2(d) illustrates the temporal evolution of the Nusselt number Nucalculated using grid resolutions of 25 × 100, 50 × 200, 100 × 400, and 200 × 800. The results indicate that the solution obtained with the 100 × 400 grid deviates by less than 3% from that of the finest grid (200 × 800), whereas the coarser grids (25 × 100 and 50 × 200) exhibit larger discrepancies. Therefore, the 100 × 400 grid was adopted for all subsequent simulations to ensure a balance between computational accuracy and efficiency.

2.2. Prediction via machine learning algorithms

To address the limitations of traditional modeling techniques and explore the potential of advanced predictive tools, this study proposes a comprehensive machine learning framework for predicting the thermal performance of nano-enhanced PCM-based BTMS. A high-fidelity simulation dataset comprising 343 cases with varied nanoparticle distribution patterns was constructed using LBM simulation. One of the latest ML algorithms for small tabular datasets, namely TabPFN, is implemented to establish accurate surrogate models capable of capturing the nonlinear interactions between design variables and thermal behavior. It serves as the benchmark model and is compared to several popular ML models, including XGBoost, CatBoost, and BPNN. To further improve model transparency and physical interpretability, SHAP (SHapley Additive exPlanations) analysis was conducted to quantitatively identify and rank the influence of key input features.

2.2.1. Tabular data prior-data Fitted Network (TabPFN)

TabPFN is a transformer-based foundation model tailored specifically for small-scale tabular data tasks, including both regression and classification [65]. Unlike traditional su-pervised learning methods such as XGBoost, CatBoost, and conventional neural networks, which require extensive task-specific training and hyperparameter tuning, TabPFN exploits in-context learning (ICL) to perform inference in a single forward pass, eliminating the need for additional training.

During inference, given a training set $(x_i, y_i)_{i=1}^{n}$ and a test example x_{test}, TabPFN produces predictions as:

$$\hat{y} = q_{\theta(}\, y|x_{test}, \{(x_i, y_i)\}_{i=1}^{n}\,) \tag{27}$$

where, q_θ is the transformer-parameterized approximation of the posterior predictive distribution, and θ is the pretrain weight learned in pretrain step.

A key factor behind TabPFN's performance lies in its use of synthetic pre-train datasets that simulate the causal structure and feature correlation of real-world tabular data. To generate such datasets, researchers employ structural causal models (SCMs), which offer a principled framework for capturing the generative and causal relationships within data. At pre-train step, learning to approximate the posterior predictive distribution over synthetic datasets $D \sim p(D)$

$$p(y|x, D) = \int p(y|x, D)p(t|D)dt \tag{28}$$

TabPFN's pre-training then minimizes the PFN loss—the expected negative log-likelihood over held-out synthetic targets—so that $q_\theta \approx p$. Formally:

$$l_\theta = \mathbb{E}_{D\cup x,y\sim p(D)}[-\log q_\theta(y|x, D)]. \tag{29}$$

TabPFN leverages ICL, the same paradigm that has driven the success of large language models, to learn robust tabular prediction algorithms entirely through 2D-aware transformer architectures that alternates attention across rows and columns. Although ICL was initially discovered in language models, recent studies [66–69] have shown that transformers can also learn simple algorithms such as logistic regression. Furthermore, Prior-data Fitted Networks (PFNs) have demonstrated that even complex algorithms, i.e., Gaussian Processes and Bayesian Neural Networks, can be approximated via ICL. This extends the model's applicability to a wide range of learning tasks, including those without closed-form solutions.

2.2.2. Other ML models for the purpose of comparison

In addition to TabPFN, several widely used and well-established machine learning models are adopted for comparison in this study. These models, including XGBoost, CatBoost, and Backpropagation Neural Networks (BPNNs), have demonstrated excellent performance in various engineering and scientific prediction tasks, particularly for modeling complex nonlinear relationships and high-dimensional feature spaces [44,70]. Their proven predictive capabilities and extensive adoption in the literature make them suitable benchmarks for evaluating the effectiveness and advantages of the proposed TabPFN-based framework.

Neural networks, inspired by biological neural networks, were first proposed in 1943 by Warren McCulloch and Walter Pitts [8]. The information would be labelled before being fed into the input layer (X) and the predicted data would be ultimately exported from the output layer (Y) via a number of in-between layers, namely the hidden layer, which allows for more complex features to be interpreted or extracted from the initial input. This "black box" architecture facilitates the extraction of intricate details. In this study, to provide a more comprehensive picture of the PCM performance prediction, a multi-output BPNN was adopted. A schematic diagram of inputs and outputs based on BPNNs algorithms are shown in Fig. 3.

Extreme gradient boosting (XGB), introduced by Chen and Guestrin [71], is a sophisticated supervised machine learning technique grounded in the decision tree methodology. In contrast to the gradient boosting framework, the loss function in XGB is regularised within the objective function, facilitating the smoothness of the final learning weights and diminish ing the likelihood of overfitting. Details of this method can be found in our previous study [70].

CatBoost is a gradient boosting algorithm developed to handle categorical features more efficiently without extensive preprocessing. It uses ordered boosting and innovative tech niques like target statistics to reduce overfitting, making it well-suited for datasets with high-cardinality categorical variables [72]. Details of this method can be found in our previ ous study [73].

2.2.3. Model interpretability

Although ML-based surrogate modeling generally offers great predictive accuracy, they are regarded as black boxes, which lack comprehensiveness in their internal working mecha-nisms, i.e., how particular features affect the output and whether these effects are positive or negative. To address this concern, this study adopted an interpretability analysis method, namely SHapley Additive exPlanations (SHAP) analysis.

SHAP method is based on Shapley value theory, which ensures the consistency and fairness of each feature's contribution [74]. This method estimates the contribution of each input feature to a specific sample by comparing two models: one that includes the feature and one that excludes it. The difference in their outputs quantifies the feature's contribution to that sample. The overall importance of each feature across the entire dataset is then determined by calculating the weighted average of its contributions over all samples. The calculation of SHAP values is as follows:

$$f(\mathrm{X}') = \mathrm{J}_0 + \sum_{\mathrm{i}=1}^{\mathrm{K}} \mathrm{J_i X_i} \tag{30}$$

where f is an interpretation model; X indicates whether input parameter i is present in the set of input parameters, and i is in the set of input parameters ($X_i' = 1$), i is not in the set of input parameters ($X_i' = 0$); J is the attribution of input parameters; K is the number of input parameters.

2.2.4. Evaluation metrics and hyperparameter determination

In this study, to evaluate the predictive model performance, three widely adopted error metrics were used, namley Mean absolute Error (MAE), Root Mean Squared Error (RMSE) and R-squared (R^2).

Table 3
Optimized hyperparameters for different ML models.

Model	Hyperparameters
Regression NN	Hidden layers: 3 (128–128–64), ReLU activation Dropout: 0 Batch size: 32 Optimizer: Adam, lr = 10^-3 Weight decay: 0 Scheduler: ReduceLROnPlateau (patience = 50) Early stopping: 100 epochs Loss: MSE
CatBoost	Iterations: 20,000 Loss and eval_metric: MultiRMSE Learning rate: 0.05 Depth: 4 L2 leaf reg: 1 Colsample_bylevel: 0.7 Bayesian bootstrap: True Bagging temperature: 1 Boost from average: False Leaf estimation: Gradient
XGBoost	Alpha: 0 Gamma: 0 Learning rate: 0.05 Max depth: 4 Reg lambda: 10 Colsample_bytree: 0.7 Subsample: 0.6 Min child weight: 1 Max delta step: 0 N estimators: 500

$$MAE = \frac{1}{n}\sum_{i=1}^{n} |y_i - \hat{y}_i| \tag{31}$$

$$RMSE = \sqrt{\frac{1}{n}\sum_{i=1}^{n} (y_i - \hat{y}_i)^2} \tag{32}$$

$$R^2 = 1 - \frac{\sum (y_i - \hat{y})^2}{\sum (y_i - \bar{y})^2} \tag{33}$$

Hyperparameter tuning was performed using Grid search, which exhaustively tries every combination of values of specified parameter values. In this study, to ensure consistency across all baseline models, the dataset was first partitioned by holding out 25% as the test set. The remaining 75% was designated as the development set, within which 10% was used for validation and 90% for training, resulting in a split of 67.5%/7.5%/25% for training/validation/test, respectively. We use TabPFN in its standard inference-only regime: the pretrained model receives the training split as the in-context support set, and each test instance is treated as a query. No fine-tuning is performed and test instances are never used as context.

To prevent overfitting, a range of strategies was employed across the evaluated mod els. For XGBoost, the training objective was set to reg: squarederror (optimizing RMSE), with overfitting controlled by early stopping on validation RMSE (patience = 50) under a large n estimators upper bound. Additional regularization was introduced through shal low trees (max depth = 4), column subsampling (colsample bytree = 0.7), row subsampling (subsample = 0.6), and L2 regularization (reg lambda = 10). For CatBoost, RMSE was used as both the training loss and evaluation metric, with overfitting mitigation achieved via early stopping on validation RMSE, Bayesian bootstrap, bagging temperature for stochastic regularization, tree depth fixed at 4, column subsampling (colsample bylevel = 0.7), and L2 regularization (l2 leaf reg = 1). For the regression neural network baseline, we adopted a 128–128–64 multilayer perceptron (MLP) with ReLU activation and batch size of 32, trained using MSE loss. Overfitting control involved early stopping on validation loss (patience ≈ 100), ReduceLROnPlateau to adjust the

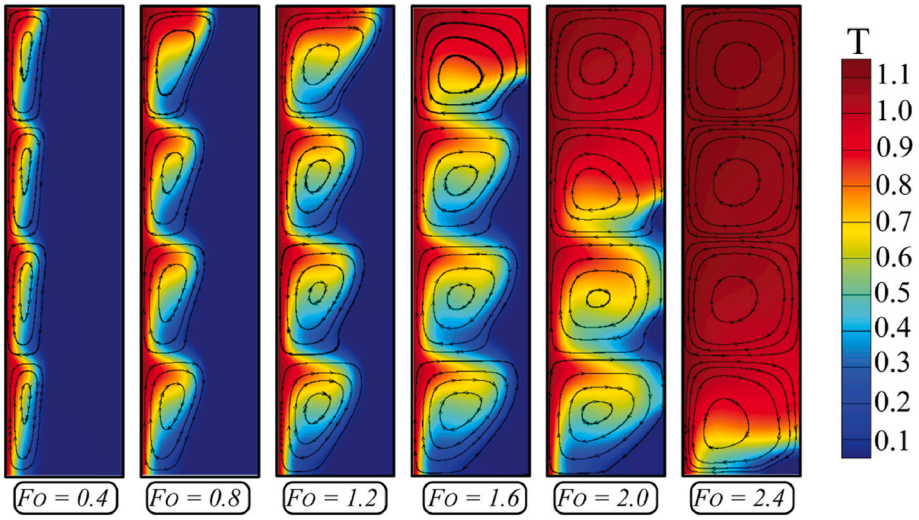

Fig. 4. The dynamic temperature contours of uniform distribution at a given time step.

learning rate (patience ≈ 50), modest model capac ity, and standardization applied on the training set for both inputs and per-target outputs.

Furthermore, weight decay and dropout were explored in ablation experiments but were not retained in the final configuration. Detailed hyperparameters used for BPNN, XGBoost, and CatBoost are outlined in Table 3.

3. Results and discussions

This section presents an analysis of the nano-PCM cooling

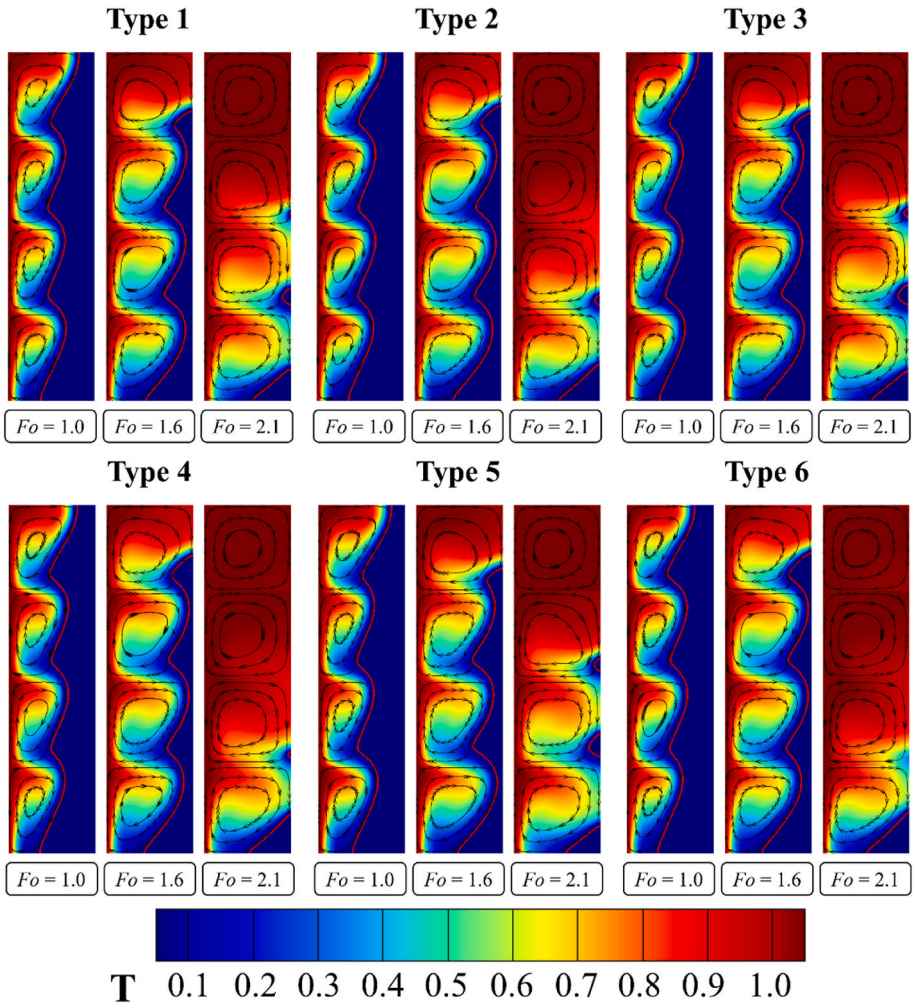

Fig. 5. The dynamic temperature contours of different type at: *Fo* = 1.0, 1.6 and 2.1.

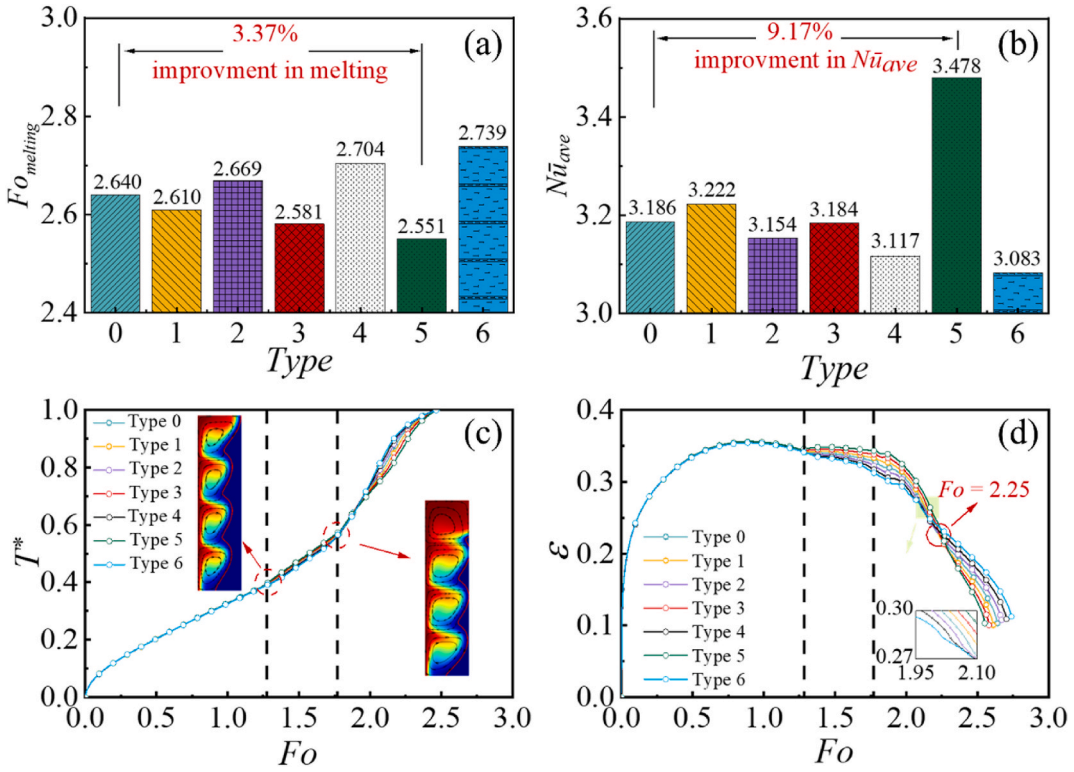

Fig. 6. Comparative analysis of PCM melting performance for different structural types: (a) Total melting time $Fo_{melting}$; (b) Temperature (T^*) ; (c) Temperature absolute deviation (ε); (d) Average Nusselt number, Nu_{avg}

performance and the corre sponding machine learning predictions. The initial part focuses on the thermal behavior of nano-PCM systems under various nanoparticle distribution patterns. A comprehensive and robust dataset was constructed based on these simulations to serve as the foundation for predictive modeling. Several machine learning algorithms were then employed to forecast the thermal response of nano-PCM systems. The predictive accuracy of different models was systematically compared, and a SHAP analysis was conducted to interpret the influence of nanoparticle arrangements on PCM performance, which aims to provide physical insight into key factors governing nano-PCM performance.

3.1. Nano-PCM cooling performance

This study first investigates the heat transfer dynamics of phase change material (PCM) with a 5% volume fraction uniformly distributed throughout the domain. Fig. 4 presents the temporal evolution of the temperature contours and natural convection patterns. It is evident that the liquid PCM experiences non-uniform heating between the left and right sides, resulting in asymmetric buoyancy forces that drive clockwise circulations within each region. These convective flows enhance heat transfer, especially in the upper parts of each region where higher temperatures are observed, consistent with the findings reported by Jilte et al. [75]. This elevated temperature promotes deeper heat penetration. Consequently, the liquid–solid interface within each region appears as a right-tilted straight line, and the overall solid–liquid boundary across the PCM exhibits a rightward-sloping wavy pattern. Additionally, in the upper parts of the lower regions, the high-temperature PCM moving rightward transfers heat upward, causing the upper regions to become hotter than the lower ones. At a $Fo = 1.2$, the solid–liquid interface in the upper part of Region 1 reaches the far-right boundary, indicating a reduction in the PCM's heat storage capacity. By $Fo = 2.0$, the PCM in Region 1 has completely melted and experiences a rapid temperature rise. At $Fo = 2.4$, the upper three regions near the heating surface exhibit uniformly high temperatures, while low-temperature zones still persist in Region 4.

A key challenge of uniformly distributed nano-PCM is the tendency for heat to accumulate in the upper regions, leading to rapid full melting of the PCM, latent heat saturation, and consequently a loss of phase-change heat storage capability. Meanwhile, the lower regions absorb heat too slowly, leading to uneven melting and reduced overall efficiency. To enhance downward heat transfer, various nanoparticle distribution strategies listed in Table 2 are explored, and the corresponding results are presented in Fig. 5. It shows that for the same average nanoparticle content in the PCM, strategies that introduce additional nanoparticles in Region 4 (Type 1, Type 3, and Type 5) enable the PCM to absorb heat more uniformly. This indicates that increasing the nanoparticle concentration in the lower region can alleviate the insufficient heat absorption there, thus reducing the thermal burden on the upper regions and accelerating the overall melting process.

From the above contour analysis, it is evident that, in addition to the excellent latent heat absorption capacity of the PCM, convective heat transfer plays a significant role. It not only affects the overall heat absorption process but also governs the temperature distribution within the system. To quantitatively evaluate the strength of convective heat transfer, the time-averaged Nusselt number is introduced as an indicator, calculated using the following equation:

$$Nu_{\mathrm{avg}} = \frac{1}{Fo_{\mathrm{melting}}} \int_0^{Fo_{\mathrm{melting}}} Nu(Fo)\,dFo \tag{34}$$

The temperature standard deviation of the PCM, denoted as ε, is calculated to using the following equation to evaluate the degree of temperature uniformity within the PCM:

$$\varepsilon = \sqrt{\frac{\int_V \left(T^* - T^*_{ave}\right)^2 dV}{\int_V dV}} \tag{35}$$

Fig. 6 quantitively investigates the cooling performance of the PCM

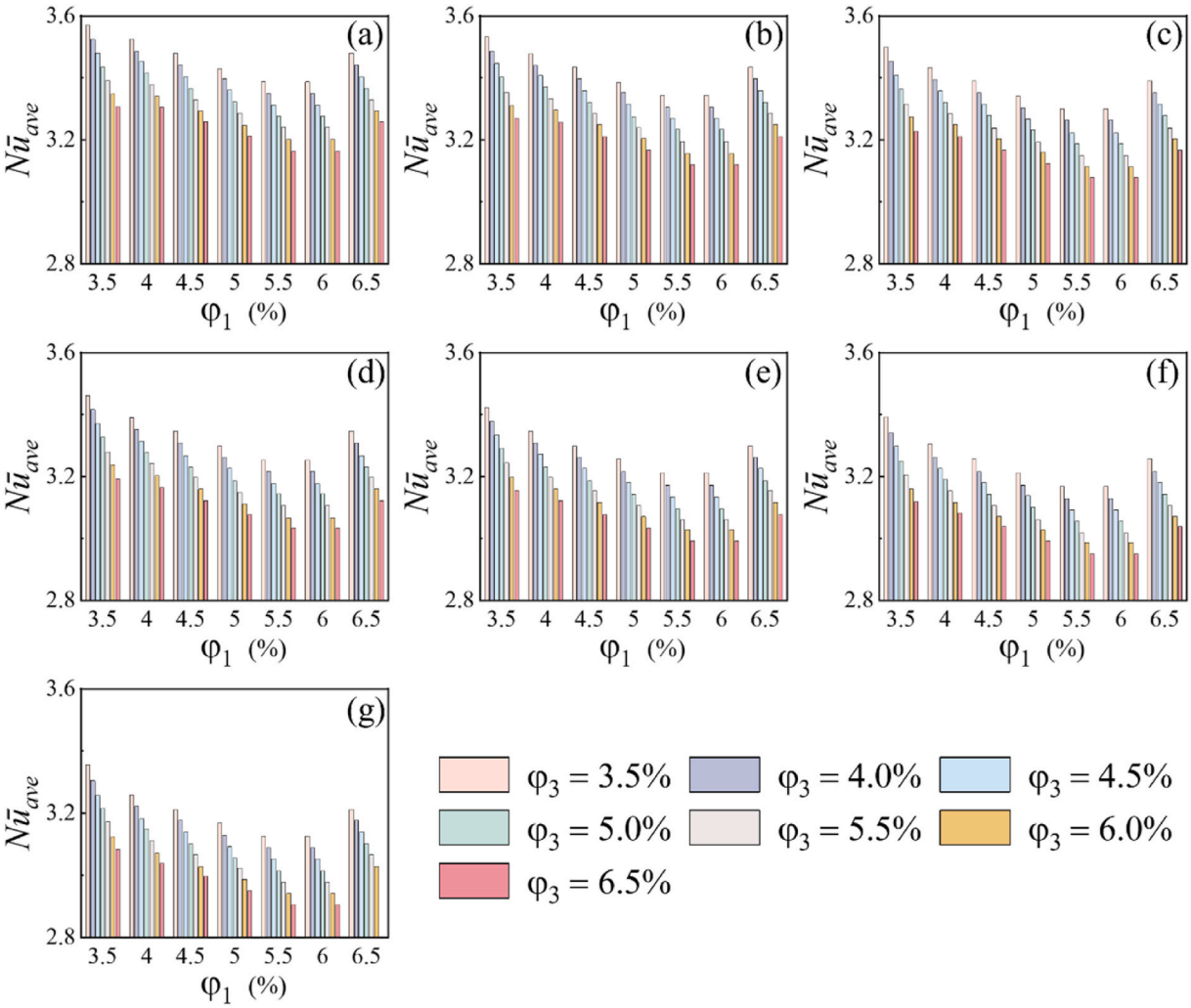

Fig. 7. The variations of Fomelting with various distributions of φ_1: (a) $\varphi_1 = 3.5\%$, (b) $\varphi_1 = 4.0\%$, (c) $\varphi_1 = 4.5\%$, (d) $\varphi_1 = 5.0\%$, (e) $\varphi_1 = 5.5\%$, (f) $\varphi_1 = 6.0\%$, and (g) $\varphi_1 = 6.5\%$, from left to right.

under different nanoparticle distribution strategies. Figure 6(a) shows that the total melting times for Types 0 to 6 are 2.64, 2.61, 2.70, 2.58, 2.70, 2.55, and 2.74, respectively. By carefully designing the nanoparticle distribution, the PCM melting process can be accelerated by up to 3.37% when the negative gradient arrangement (Type 5) is adopted. Figure 6(b) illustrates the average Nusselt number (Nu_{avg}). It shows that dispersed nanoparticle arrangements (Type 1 and Type 5) enhance overall convective heat transfer. Compared to the uniform distribution, Type 5 increases the average Nusselt number by 9.17%. Fig. 6(c) shows the temperature variation with the Fourier number (*Fo*). Two inflection points are observed in the temperature rise rate. The first inflection occurs at $Fo = 1.27$, when the uppermost solid–liquid interface in Region 1 reaches the right boundary, causing the temperature rise rate to increase from 0.24 to 0.35. The second inflection occurs at $Fo = 1.77$, when the PCM in Region 1 is nearly fully melted and its temperature approaches that of the heating surface, indicating a complete loss of heat dissipation capacity. As a result, the temperature rise rate further increases to 0.54. Toward the end of melting, the temperature increase slows down due to the reduced temperature difference between the PCM and the heating surface. Figure 6(d) displays the temporal evolution of temperature uniformity. The temperature standard deviation, ε, is initially low due to the uniform initial temperature. It then increases as a result of interregional heat transfer. After $Fo = 1.19$, ε gradually decreases as the temperature in all regions of the PCM approaches that of the heating surface. After $Fo = 2.36$, Type 5 achieves the best temperature uniformity, which reaches 0.10 by the time it completely melts.

The above results demonstrate that the strategic arrangement of nanoparticle distribution can effectively enhance the cooling performance and promote heat dissipation uniformity. To provide a more thorough and comprehensive evaluation of PCM configurations, this study analyzes 343 arrangement cases as described in the methodology section.

Fig. 7 shows the complete melting time for various nanoparticle distributions within the PCM. When the average volume fraction of the nanoparticle is 5% throughout the PCM, increasing the concentration in Region 1, Region 2, or Region 3 slows the melting process. This indicates that enhancing the concentration in Region 4 significantly accelerates the melting process and assumes a dominant role in the overall thermal response. This effect stems from the significantly enhanced thermal conductivity in Region 4, which enables greater local heat absorption at the bottom. Consequently, Region 4 governs the overall heat transfer pathway, offsets heat losses toward the upper regions, and ensures a more efficient and balanced melting process across the entire PCM domain. Among all tested cases, the configuration with a nanoparticle distribution of 3.5%, 3.5%, 3.5% and 9.5% from top to bottom (Regions 1 to 4) achieves the fastest heat dissipation, with an acceleration rate of 13.08%.

Fig. 8 presents the average Nusselt number across all nano-PCM configurations. It is observed that increasing the nanoparticle

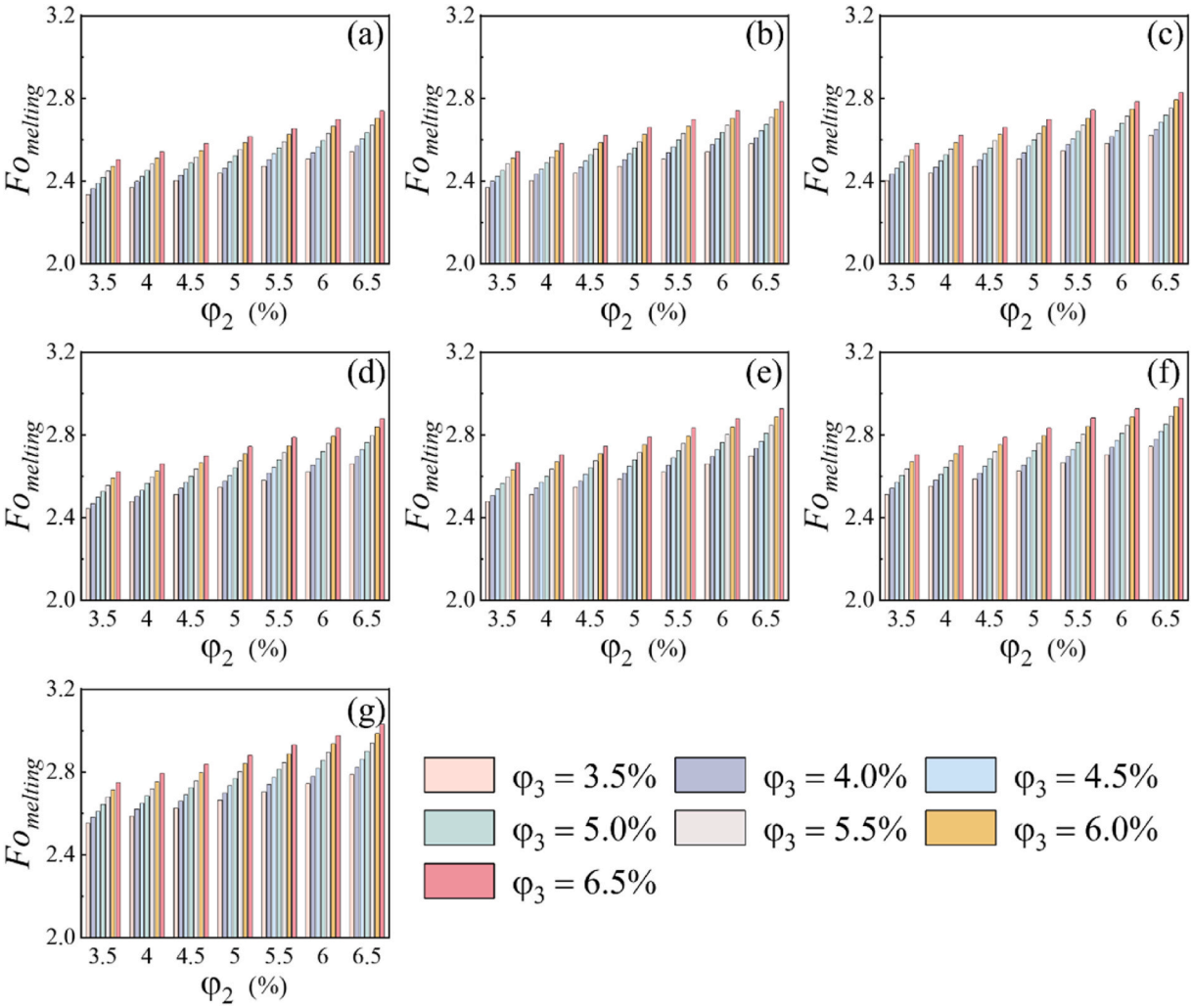

Fig. 8. The variations of time-averaged Nusselt number with various distribution: (a) $\varphi_2 = 3.5\%$, (b) $\varphi_2 = 4.0\%$, (c) $\varphi_2 = 4.5\%$, (d) $\varphi_2 = 5.0\%$, (e) $\varphi_2 = 5.5\%$, (f) $\varphi_2 = 6.0\%$, (g) $\varphi_2 = 6.5\%$.

concentration in the middle regions (Regions 2 and 3) leads to a decrease in the overall Nusselt number. This occurs because reducing the concentration in Regions 1 and 4—where heat transfer plays a more dominant role—has a greater adverse effect on global thermal performance. Specifically, during the early melting stage, the lower regions enhance upward convective transport, while in the later stage, after the upper PCM has fully melted and lost its latent heat absorption capacity, it begins to transfer heat downward. In contrast, the middle regions primarily function as flow channels, and their enhanced thermal conductivity contributes less to the overall convective heat trans fer. Therefore, to enhance heat transfer under a fixed total nanoparticle concentration, it is preferable to allocate more nanoparticles to the end regions. Additionally, it is noted that when the nanoparticle concentration in Region 1 (φ_1) becomes excessively high (e.g., 6.5%), the corresponding decrease in φ_4 leads to a reduction in *Nu*. This indicates that, between the two end regions, the bottom (Region 4) plays a more critical role in sustaining upward convective heat transport and thus exerts a dominant influence on the global heat transfer performance. Among all tested cases, the configuration with a nanoparticle distribution of 3.5%, 3.5%, 3.5%, and 9.5% from top to bottom (Regions 1 to 4) yields the highest Nusselt number of 3.57.

3.2. Machine learning results

The LBM simulations above provide valuable insight into heat dissipation behavior and also yield a robust dataset. To further compare the heat transfer performance of nano-PCMs with different spatial arrangements, we calculated their cooling power, defined as follows:

$$P_{cool} = \frac{C_p \cdot m \cdot \Delta T + L \cdot fl}{Fo} \tag{36}$$

where C_p denotes the specific heat capacity, L represents the latent heat, and fl indicates the liquid fraction. To better highlight and demonstrate the impact of nanoparticle arrangement, the cooling power ratio and sigma ratio are defined as the ratios of the cooling power and temperature standard deviation under a given distribution to those under the uniform distribution.

In this study, four ML models were employed, i.e., BPNN, XGBoost, CatBoost, and TabPFN, to predict the heat transfer performance of the nano-PCMs. The input features are the nanoparticle volume fractions in four spatial regions. The outputs include: the complete melting time, cooling power ratio, sigma ratio, and average Nusselt number. Fig. 9 displays the correlations of the predictions based on the training dataset for each evaluated model, as represented by the R^2 values. It can be found that for the training dataset, all four models exhibited very good predictive accuracy, with R^2 values significantly exceeding 99%. However, it is worth mentioning that among the four models, BPNN yielded the worst outcomes, especially when predicting the sigma ratio, as the R^2 value was only 0.894. TabPFN, XGBoost, and CatBoost all capture the nonlinear relationships between the input features and the predicted

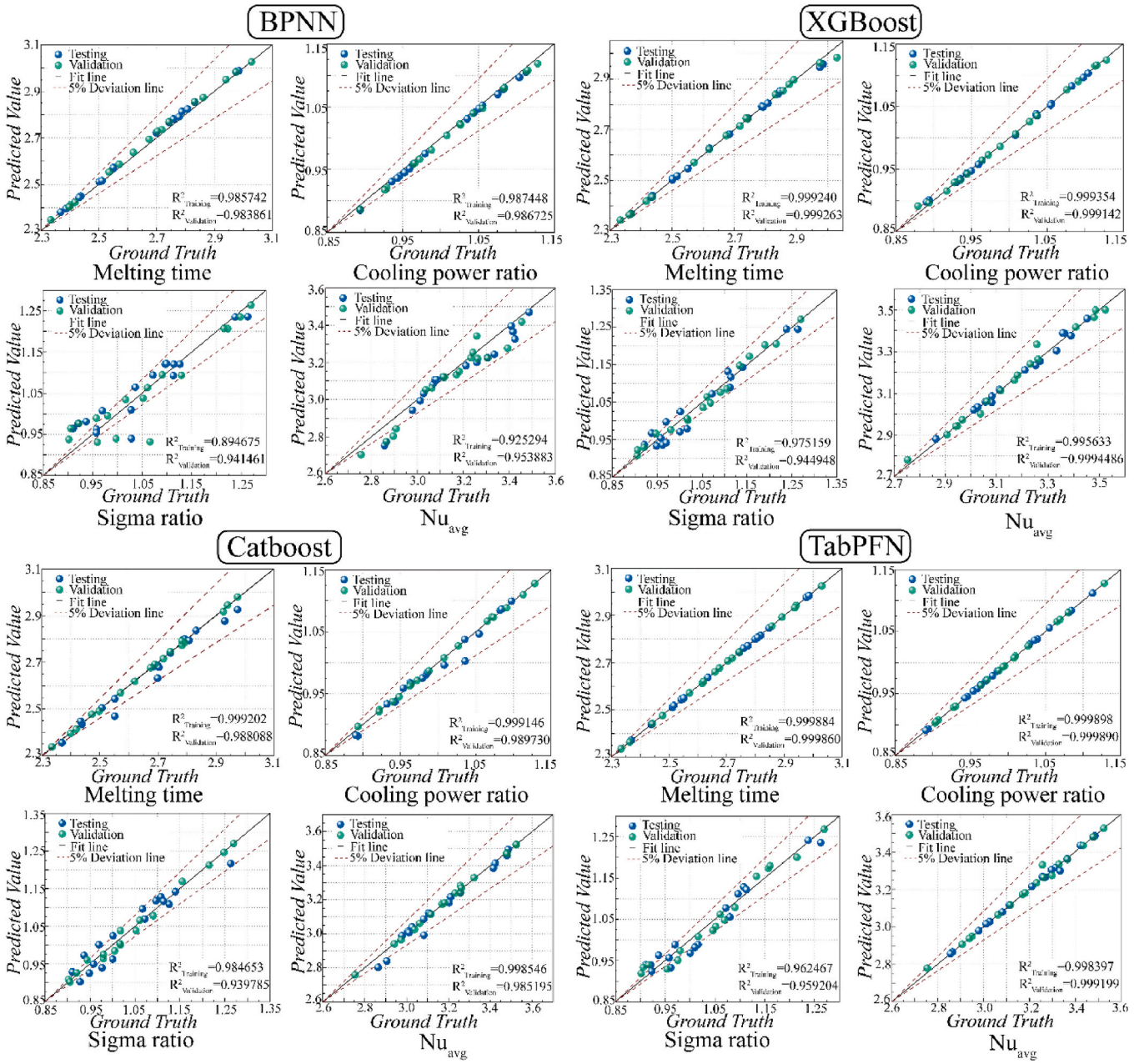

Fig. 9. The correlations between the LBM results and prediction by different ML models.

physical quantities, with TabPFN performing significantly better, with its R^2 ranging from a minimum of 0.9592 to nearly 1. Most impressively, TabPFN demonstrated outstanding predictive capability for melting time, cooling Power Ratio, and Nu_{avg}, achieving R^2 values consistently above 0.998. These results are significantly higher than those reported in other PCM-BTMS studies. For instance, compared with the work of Khaboshan et al. [76], who investigated BTMS configurations with fins, metal foam, and PCM and achieved R^2 values of $0.98 - 0.99$ using an ANN model, TabPFN attains even higher goodness of fit. This highlights the distinct advantage of TabPFN in the $PCM - BTMS$ domain.

Fig. 10 presents the histograms of prediction errors for the four ML algorithms during training. It is evident that the magnitude and distribution of errors differ significantly among the models. For instance, Fig. 10(a) highlighted that while predicting Nusselt number, BPNN exhibits a relatively wide error range within $\pm 0.2(10^{-1})$. In comparison, for tree based ML models (i.e., XGBoost and Catboost), they show much narrow error distributions, confined within $\pm 0.5 \times 10^{-2}$. TabPFN demonstrates the most concentrated error distribution, with errors limited to $\pm 1.0 \times 10^{-3}$, highlighting its superior prediction capability and stability. Similar trends can also be observed for the sigma ratio (Fig. 10(b)), cooling power ratio (Fig. 10(c)), and melting time (Fig. 10 (d)), further confirming that TabPFN consistently yields the lowest prediction errors across different physical quantities.

To compare the predictive performance of different models across various indicators, the MAE values were calculated, as shown in Fig. 11. All four models achieved the highest ac-curacy in predicting the cooling power ratio, with MAE and RMSE ranging from 4.7×10^{-4} to 3.36×10^{-3} and 5.47×10^{-4} to 5.38×10^{-3}, respectively. In contrast, the prediction of Nuavg was relatively less accurate. TabPFN consistently outperformed the other models across all targets. For instance, it reduced the MAE for Melting Time by approximately 48%, 84%, *and* 91% compared to XGBoost, CatBoost, and BPNN, respectively. For Cooling Power Ratio, the improvements reached about 56%, 86%, and 91%, while for Nuavg the reductions were even more pronounced, at

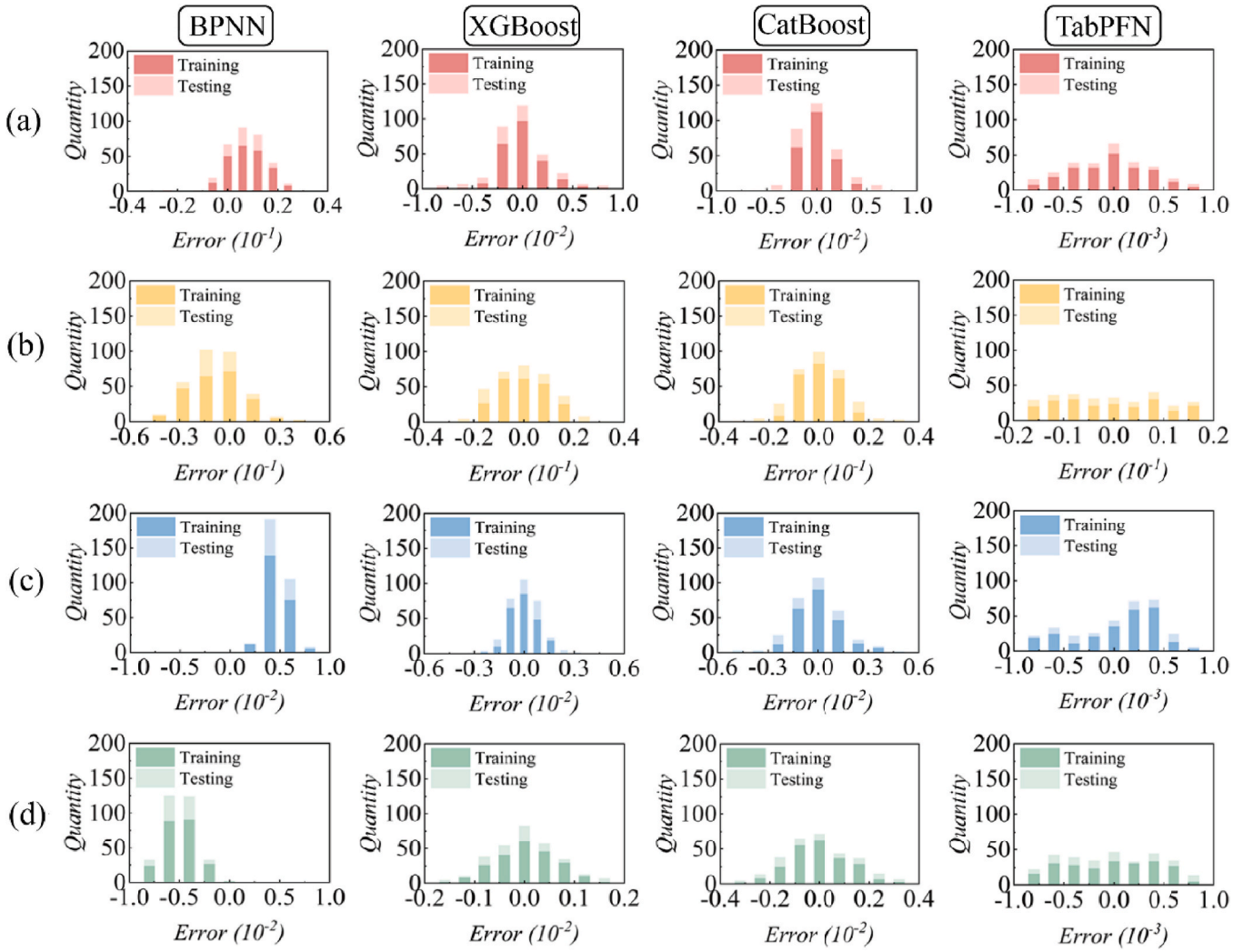

Fig. 10. Histogram Analysis of Prediction Errors by four ML algorithms: (a) Nu_{avg}; (b) Sigma ratio; (c) Cooling power ratio; (d) Melting time.

67%, 80%, and 92%. Even for Sigma Ratio, where overall errors were lower, TabPFN still yielded a reduction of 8 – 21%. Most impressively, for Nu_{avg}, TabPFN reduced the MAE by approximately 67%, 80%, and 92% relative to XGBoost, CatBoost, and BPNN, respectively. When benchmarked against prior studies in the PCM – BTMS domain, TabPFN further highlights its superiority. For example, Gu et al. [42] introduced a BKA–Convolutional Neural Network (CNN)–Self Attention (SA) model for battery temperature prediction and reported an RMSE of 0.131. By comparison, our TabPFN achieves markedly better predictive performance across multiple physical tar gets, with RMSE values ranging from approximately 0.001 to 0.033. These results indicate that TabPFN not only achieves lower error metrics in terms of magnitude within this work, but also substantially outperforms existing studies, thereby confirming its superior generalization ability and robustness in predicting complex multiphysics outputs for PCM – BTMS applications.

This study further employed SHAP analysis to perform multi-parameter sensitivity analysis and enhance the interpretability of the black-box model. Specifically, SHAP was used to quantify the contributions of the four regional concentration features to the four predicted physical quantities, as shown in Fig. 12. Feature importance is ranked by the mean absolute SHAP values. It reveals that φ4 has the highest sensitivity across all four predicted physical quantities—cooling performance, melting time, Nu_{avg}, and sigma ratio—with SHAP values consistently ranging from 0.105 to 0.410. This indicates that the model predictions are most responsive to variations in φ4, underscoring its dominant role in shaping the ma chine learning model's thermal predictions. Such sensitivity is consistent with the underlying physics captured by the LBM simulations, where Region 4 consistently undergoes the latest melting and exhibits the largest thermal gradients due to buoyancy-driven convection. In addition, SHAP analysis demonstrates that each input feature not only exhibits varying levels of importance across the four predicted targets but also exerts clear directional influences on the model outputs. The asymmetric distribution of red (high feature values) and blue (low feature values) points along the SHAP axis highlights the presence of pronounced nonlinear relationships between the inputs and the predictions, reflecting the model's ability to capture complex, non-monotonic dependencies. Specifically, for φ_4, higher values (red points) are predominantly linked to positive SHAP contributions, while lower values (blue points) are associated with negative contributions. This indicates that increasing φ_4, generally enhances *Nu*, while decreasing φ_4 suppresses it—fully consistent with the numerical mechanism that strengthening thermal conductivity at the bottom promotes buoyancy-driven upward convection and thereby improves overall heat transfer performance. By contrast, φ_2 and φ_3 show much lower importance (mean|SHAP| ≈ 0.047 and 0.214, respectively), with most of their SHAP contributions lying on the non-positive side. This suggests that increasing nanoparticle concentration in the middle regions is generally unfavorable for enhancing *Nu*, consistent with the observation in Section 3.2 that these regions primarily act as flow channels, where improved conductivity contributes

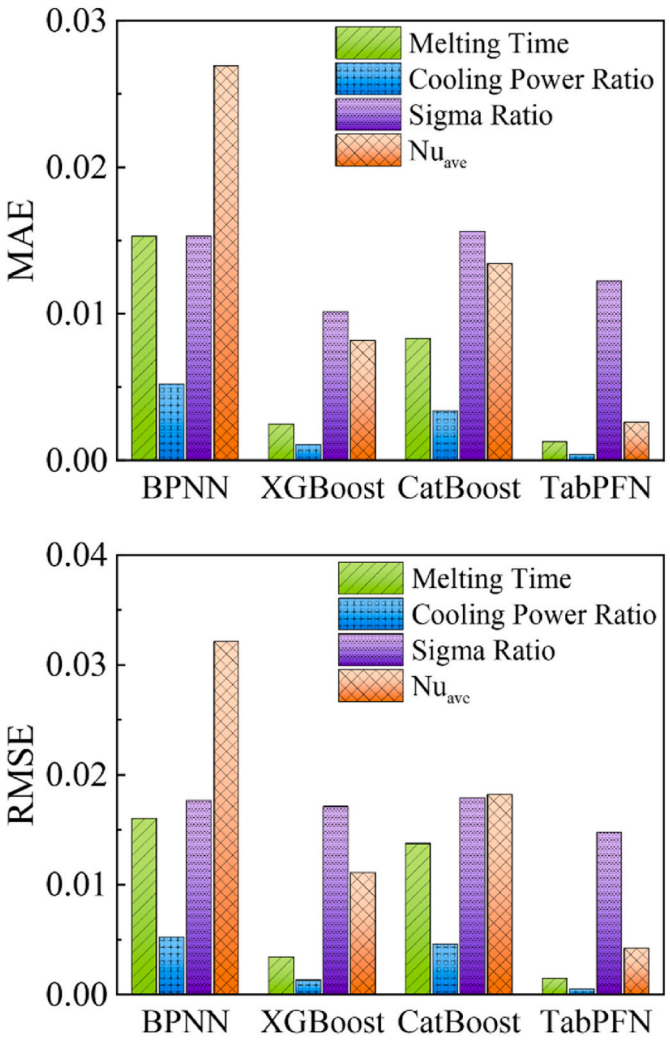

Fig. 11. MAE and RMSE quantification of the prediction models.

little to the global convective heat transfer.

4. Conclusion

In this study, a zonal nanoparticle distribution strategy was proposed to alleviate local heat accumulation induced by PCM convection for battery thermal management. A total of 343 nano-PCM configurations were systematically examined using the well-validated Lat-tice Boltzmann method. Based on this dataset, an explainable predictive framework was developed that incorporated several machine learning models, including BPNN, XGBoost, CatBoost, and the state-of-the-art TabPFN, to estimate multiple evaluation metrics such as melting time, cooling power ratio, and sigma ratio. TabPFN was further benchmarked against these widely used methods, and SHAP analysis was employed to interpret the model and provide physical insights into the influence of different nanoparticle distributions. The main findings are summarized as follows.

- LBM simulation results indicate that stratified nanoparticle distribution effectively mitigates thermal accumulation. In particular, higher nanoparticle concentrations in the lower region significantly enhance the overall thermal performance. With nanoparticle fractions of 3.5%,3.5%,3.5%, and 9.5% from region 1 to 4, the average Nusselt number increases by 12.04%, and the melting time decreases by 13.08%.
- TabPFN exhibited exceptional prediction accuracy in comparison to those popular models such as BPNN, XGBoost, and CatBoost. The error bins during training were generally lower in magnitude, which undersores its enhanced accuracy and resilience. TabPFN attained reductions in MAE between 8% and 92% and reductions in RMSE between 7% and 90 % for various target variables. These significant enhancements highlight TabPFN's robust generalisation capability and its promise as a dependable surrogate model for intricate multiphysics prediction applications.
- SHAP analysis revealed that φ4 played a dominant role across all predicted targets, which effectively visualizes and quantifies its strong influence on convective behavior and heat retention in BTMS. This enhanced interpretability is expected to deepen the understanding of the internal workings of models and further provide potential insights into the nonlinear and non-monotonic relationships between regional concentration distributions and key performance metrics.

This study introduces a lightweight, data-efficient modeling framework based on LBM datasets for battery thermal management and highlights the physical insights gained from interpretable machine learning. The proposed approach is expected to serve as a valuable tool for guiding optimal nano-PCM design in practical energy systems, which could support industrial implementation in future electric vehicle applications. Nonetheless, several limitations should be acknowledged, and corresponding future work remains necessary: (1) extending the LBM model to 3D simulations and batch calculations at the battery module level to better capture system-level complexities; (2) incorporating experimental studies to strengthen the reliability and practical feasibility of the proposed strategy; and (3) address production feasibility (manufacturability, cost, energy density, PCM stability) and validate performance under extreme operating scenarios (fast charging/high-rate pulsing) to enhance robustness, generalizability, and industrial applicability. Efforts to resolve these challenges will not only strengthen the framework itself but also help advance the development of re liable, scalable, and industry-ready solutions for battery thermal management in electric vehicles, thereby supporting large-scale adoption and practical implementation.

CRediT authorship contribution statement

Bichen Shang: Writing – original draft, Methodology, Formal analysis, Data curation. **Guo Li:** Software, Formal analysis, Data curation. **Weijie Sun:** Methodology, Investigation, Data curation, Conceptualization. **Liwei Zhang:** Visualization, Validation, Methodology, Formal analysis, Data curation. **Guanzhe Cui:** Writing – review & editing, Methodology. **Jiyuan Tu:** Writing – review & editing, Supervision. **Xiang Fang:** Writing – review & editing, Supervision, Formal analysis, Conceptualization. **Xueren Li:** Writing – review & editing, Writing – original draft, Supervision, Conceptualization.

Declaration of competing interest

The authors declare that they have no known competing financial interests or personal relationships that could have appeared to influence the work reported in this paper.

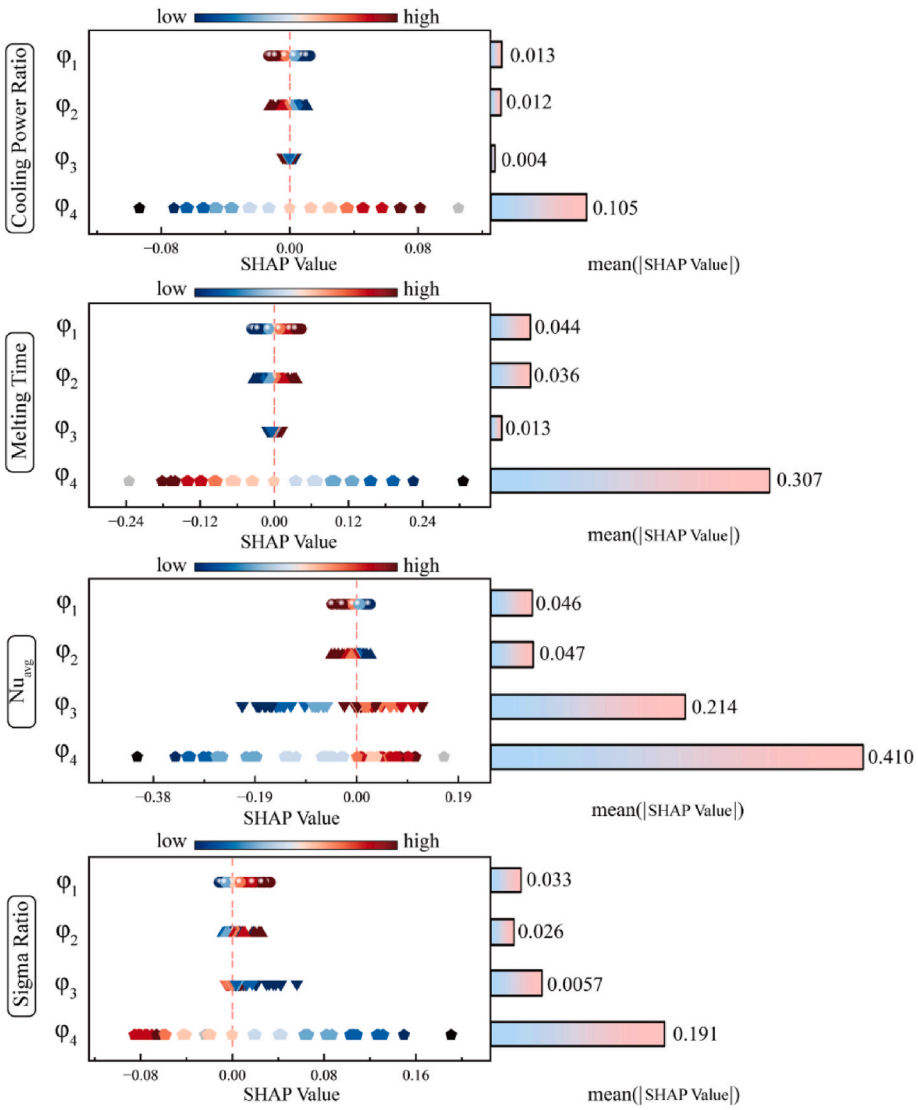

Fig. 12. SHAP summary plots showing the influence of input features ($\varphi_1 - \varphi_4$) on four performance metrics: Cooling Power Ratio, Melting Time, Nuavg, and Sigma Ratio. Feature importance is ranked by mean absolute SHAP values.

Appendix

Sensitivity analysis was conducted to further assess the reliability of the proposed model under elevated nanoparticle concentrations. For this purpose, a sedimentation factor was introduced, defined as

$$\eta = \frac{\phi_{eff}}{\phi_{\text{nom}}} \tag{37}$$

where ϕ_{eff} is the effective nanoparticle volume fraction contributing to heat transfer and ϕ_{nom} is the nominal concentration. In the baseline condition ($\varphi_{1-3} = 3.5\%,\ \varphi_4 = 9.5\% vol.$), η was perturbed to 0.95,0.90, and 0.85, representing scenarios in which 5%,10%, and 15% of the nominal nanoparticles were assumed to settle or aggregate and thus became inactive for heat transfer. As shown in the following figure, both the global liquid fraction (Fig. 13(a)) and the local liquid fraction in region 4 (Fig. 13(b)) deviated by less than 5 % under these perturbed conditions, confirming that the predicted enhancement of thermal performance remains robust even when potential sedimentation effects are considered.

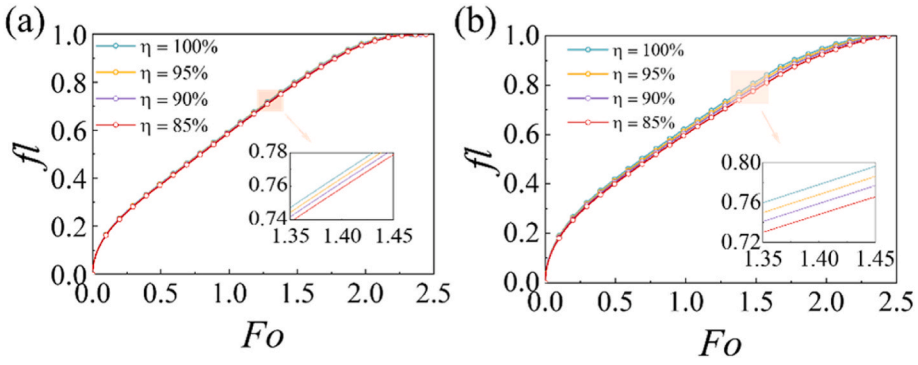

Fig. 13. Effects of introducing an effective concentration factor to mimic nanoparticle sedimentation. (a) Evolution of global liquid fraction with different effective concentrations. (b) Local liquid fraction evolution in region IV ($\varphi_4 = 9.5\%$).

Data availability

The data that has been used is confidential.

References

[1] Filonchyk Mikalai, Peterson Michael P, Zhang Lifeng, Hurynovich Volha, He Yi. Greenhouse gases emissions and global climate change: examining the influence of co2, ch4, and n2o. Sci Total Environ 2024:173359.

[2] Haghani Milad, Ghaderi Hadi, Hensher David. Hidden effects and externalities of electric vehicles. Energy Policy 2024;194:114335.

[3] Tomaszewska Anna, Chu Zhengyu, Feng Xuning, O'kane Simon, Liu Xinhua, Chen Jingyi, Ji Chenzhen, Endler Elizabeth, Li Ruihe, Liu Lishuo, et al. Lithium-ion battery fast charging: a review. ETransportation 2019;1:100011.

[4] Bernagozzi Marco, Georgoulas Anastasios, Miche Nicolas, Marengo Marco. Exper imental analysis of the influence of ambient temperature for a loop heat pipe based battery thermal management system. Experimental and Computational Multiphase Flow SEP 2024;6(3, SI):242–52. https://doi.org/10.1007/s42757-023-0185-5. ISSN 2661-8869.

[5] Tian Siyu, Wu Shiwen, Cui Shuang, Tian Yafen, Balkus Kenneth J, Zhou Long, Xiong Guoping. High-performance solid-state supercapacitors integrated with thermal management systems based on phase change materials: all in one. Chem Eng J 2022;446:136787.

[6] Olabi AG, Maghrabie Hussein M, Adhari Ohood Hameed Kadhim, Sayed Enas Taha, Yousef Bashria AA, Salameh Tareq, Kamil Mohammed, Ali Abdelka reem Mohammad. Battery thermal management systems: recent progress and challenges. Interna tional Journal of Thermofluids 2022;15:100171.

[7] Ayat Gharehghani, Moeed Rabiei, Sadegh Mehranfar, Soheil Saeedipour, Amin Mahmoudzadeh Andwari, García Antonio. Carlos Mico Reche Progress in battery thermal management systems technologies for electric vehicles. Renewable and Sustain able Energy Reviews 2024;202:114654.

[8] Sutton RS, Barto AG. Reinforcement learning: an introduction. IEEE Trans Neural Network 1998;9(5). https://doi.org/10.1109/TNN.1998.712192. 1054–1054.

[9] Kassar RE, Takash AA, Faraj J, Khaled M, Ramadan HS. Phase change materials for enhanced photovoltaic panels performance: A comprehensive review and critical analysis. Energy and Built Environment 2025;6(4):655–75. https://doi.org/10.1016/j.enbenv.2024.02.004.

[10] Yang Tianyu, Braun Paul V, Miljkovic Nenad, King William P. Phase change material heat sink for transient cooling of high-power devices. Int J Heat Mass Tran 2021;170:121033.

[11] Liu Yang, Zheng Ruowei, Li Ji. High latent heat phase change materials (pcms) with low melting temperature for thermal management and storage of electronic devices and power batteries: critical review. Renew Sustain Energy Rev 2022;168:112783.

[12] Ren Honglei, Dang Chao, Yin Liaofei, Chen Zhifeng. Optimization research on battery thermal management system based on pcm and mini-channel cooling plates. Case Stud Therm Eng 2024;53:103880.

[13] Ali Khan Shahid, Xiangrong LI, Ting Lau Kwun, Dong Kejian, He Sihong, hammadWabaidur Saikh Mo, Thakur Amrit Kumar, Zhao Jiyun. Metallic pcm-based battery thermal management system for fast charging/discharging applications. Int Commun Heat Mass Tran 2024;155:107473.

[14] Weng Jingwen, Huang Qiqiu, Li Xinxi, Zhang Guoqing, Ouyang Dongxu, Chen Mingyi, Yuen Anthony Chun Yin, Li Ao, Lee Eric Wai Ming, Yang Wensheng, Wang Jian, Yang Xiaoqing. Safety issue on pcm-based battery thermal management: material thermal stability and system hazard mitigation. Energy Storage Mater 2022;53:580–612. https://doi.org/10.1016/j.ensm.2022.09.007. ISSN 2405-8297, https://www.sciencedirect.com/science/article/pii/S2405829722004949.

[15] Li Bingbing, Zhang Liwei, Shang Bichen, Huo Yutao. Numerical investigation on heat transfer characteristics in battery thermal management with phase change material composited by toroidal porous medium. Int Commun Heat Mass Tran 2024;154:107414. https://doi.org/10.1016/j.icheatmasstransfer.2024.107414. ISSN 0735-1933.

[16] Ma Zhao, Yang Wei-Wei, Yuan Fan, Jin Bo, He Ya-Ling. Investigation on the thermal performance of a high-temperature latent heat storage system. Appl Therm Eng 2017;122:579–92. https://doi.org/10.1016/j.applthermaleng.2017.04.085. ISSN 1359-4311. d oi: 10.1016/j.applthermaleng.2017.04.085.

[17] Fu Lianyan, Wu Zhengxiang, Wu Kaiyao, Chen Weidong, Zhang Mengmeng, Huang Xin, Ma Chuan, Shao Yunlin, Ran Jinyu, Chua Kian Jon. A thermally induced flexible composite phase change material with boron nitride nanosheets/carbon nanotubes modified skeleton for battery thermal management. Appl Energy 2024;373:123899. https://doi.org/10.1016/j.apenergy.2024.123899. ISSN 0306-2619.

[18] Suo Yaohong, Tang Chengbo, Jia Qiongnan, Zhao Wenrui. Influence of pcm configuration and optimization of pcm proportion on the thermal management of a prismatic battery with a combined pcm and air cooling structure. J Energy Storage 2024;80:110340. https://doi.org/10.1016/j.est.2023.110340. ISSN 2352-152X. d oi: 10.1016/j.est.2023.110340.

[19] Zhang Liwei, Shang Bichen, Sun Weijie, Tao Yao, Li Xueren, Tu Jiyuan. Data driven optimization of nano-pcm arrangements for battery thermal management based on lattice boltzmann simulation. Energy 2024;313:133670.

[20] Ayyappa Swamy Kundrapu, Verma Saket, Bhattacharyya Suvanjan. Experimen tal and numerical investigation of nanoparticle assisted pcm-based battery thermal management system. Journal of Thermal Analysis and Calorimetry 2024;149(19):1122311237. https://doi.org/10.1007/s10973-024-13052-4. ISSN 1388-6150. d oi: 10.1007/s10973-024-13052-4.

[21] Kumar Rajesh, Gupta Anoop K. Thermal management of 3d lithium-ion pouch cell under fast discharging: a multi-scale multi-domain (msmd) framework with phase change material, nanoparticle and metal foam. Int J Heat Mass Tran 2025;242:126858. https://doi.org/10.1016/j.ijheatmasstransfer.2025.126858. ISSN 0017-9310. d oi: 10.1016/j.ijheatmasstransfer.2025. 126858.

[22] Nitsas Michael, Koronaki IP. Performance analysis of nanoparticles-enhanced pcm: an experimental approach. Therm Sci Eng Prog 2021;25:100963. https://doi.org/10.1016/j.tsep.2021.100963. ISSN 2451-9049. d oi: 10.1016/j.tsep.2021.100963.

[23] Huang Shufeng, Hu Zhihan, Chen Zhixin, Yang Dayong, Huang Weili, Zhang Bin. An experimental study on the thermal performance of a heat sink filled with porous aluminum skeleton/paraffin composite phase change material. Materials 2024;17(17):4332. https://doi.org/10.3390/ma17174332. ISSN 1996-1944. do i: 10.3390/ma17174332.

[24] Kalidasan B, Pandey AK, Saidur R, Tyagi VV. Energizing organic phase change materials using silver nanoparticles for thermal energy storage. J Energy Storage 2023;58:106361. https://doi.org/10.1016/j.est.2022.106361. ISSN 2352-152X. d oi: 10.1016/j.est.2022.106361.

[25] Shang Bichen, Zhang Liwei, Li Bingbing, Huo Yutao. Thermal energy stor age system based on nanoparticle distribution optimisation for enhanced heat trans fer. J Energy Storage 2024;80:110075. https://doi.org/10.1016/j.est.2023.110075. ISSN 2352-152X.

[26] Hayder I. Mohammed. Enhancing heat storage capacity: nanoparticle and shape op timization for pcm systems. Energy Storage 2024;6:e70078. https://doi.org/10.1002/est2.70078. ISSN 2578-4862. d oi: 10.1002/est2.70078.

[27] Wu Yangyang, Rong Jiancheng, Wang Di, Zhao Xuefeng, Meng Lan, Arici Muesluem, Liu Changyu, Yang Ruitong, Dong Li. Synergistic enhancement of heat trans fer and thermal storage characteristics of shell and tube heat exchanger with hy brid nanoparticles for solar energy utilization. J Clean Prod 2023;387:135882. ISSN 0959-6526. doi: 10.1016/j.jclepro.2023.135882, https://www.sciencedirect.com/science/article/pii/S0959652623018629.

[28] Bashirpour-Bonab Hadi. Investigation and optimization of pcm melting with nanopar- ticle in a multi-tube thermal energy storage system. Case Stud Therm Eng 2021;28:101643. https://doi.org/10.1016/j.csite.2021.101643. ISSN 2214-157X. d oi: 10.1016/j.csite.2021.101643.

[29] Kumar Narender, Pandey Chandan, Chakraborty Prodyut R. Influence of compres sion ratio in compressed extended graphite on thermo-physical properties of composite phase change material: an experimental investigation. Therm Sci Eng

Prog 2025;57:103104. https://doi.org/10.1016/j.tsep.2024.103104. ISSN 2451-9049. d oi: 10.1016/j.tsep.2024.103104.
[30] Nagendra Muppana Veera, Arif Fikri M, Samykano Mahendran, Kousik Suraparaju Subbarama, Kumar Rajamony Reji, Wan Hamzah Wan Azmi, Kadirgama Kumaran. Enhancing thermal energy storage: investigating the use of graphene nanoplatelets in phase change materials for sustainable applications. Energy Technol 2024;12(7):e202400302. https://doi.org/10.1002/ente.202400302. ISSN 2194-4288. d oi: 10.1002/ente.202400302.
[31] Tabrez Alam Md, Garg Vivek, Soni Vikash, Gupta Anoop K. Effect of enclosure design with composite/nano-enhanced/dual phase change material on melting response of latent heat storage systems. Chem Eng Res Des 2025;214:125–43. https://doi.org/10.1016/j.cherd.2024.12.027. ISSN 0263-8762. d oi: 10.1016/j.cherd.2024.12.027.
[32] Dilbaz Furkan, Selimefendigil Fatih, Oztop Hakan F. Comparisons of different cooling systems for thermal management of lithium-ion battery packs: phase change material, nano-enhanced channel cooling and hybrid method. J Energy Storage 2024;90:111865. https://doi.org/10.1016/j.est.2024.111865. ISSN 2352-152X. d oi: 10.1016/j.est.2024.111865.
[33] Raheem Sadeq Basim, Ali Basem, Abed Azher M, Al-lehaibi Moaz, Hussein A, AL bonsrulah Z, Elbashir Nasrin BM. Numerical modeling for enhanced cold storage rates through nanoparticle integration within finned tank. Results Eng 2025;25:104129. https://doi.org/10.1016/j.rineng.2025.104129. ISSN 2590-1230. d oi: 10.1016/j.rineng.2025.104129.
[34] Barthwal Mohit, Dhar Atul, Powar Satvasheel. Effect of nanomaterial inclusion in phase change materials for improving the thermal performance of heat storage: a review. ACS Appl Energy Mater 2021;4:7462–80. https://doi.org/10.1021/acsaem.1c01268. ISSN 2574-0962. do i: 10.1021/acsaem.1c01268.
[35] Mahdi Heyhat Mohammad, Mousavi Sepehr, Siavashi Majid. Battery thermal management with thermal energy storage composites of pcm, metal foam, fin and nanoparticle. J Energy Storage 2020;28:101235. https://doi.org/10.1016/j.est.2020.101235. ISSN 2352-152X.
[36] Qi Cong, Li Keao, Li Chunyang, Shang Bichen, Yan Yuying. Experimental study on thermal efficiency improvement using nanofluids in heat sink with heated circular cylinder. Int Commun Heat Mass Tran 2020;114:104589. https://doi.org/10.1016/j.icheatmasstransfer.2020.104589. ISSN 0735-1933, https://www.sciencedirect.com/science/article/pii/S0735193320301160.
[37] Bibin KS, Raj S, Jayakumar JS, Roy KKEBR. OpenFOAM modelling of single-phase and two-phase heat transfer in square ducts partially filled with porous medium. Exp. Comput. Multiphase Flow 2024;6(4):408–27. https://doi.org/10.1007/s42757-024-0189-y.
[38] He Song, Ma Zhengyuan, Deng Weizhong, Zhang Zikang, Guo Ziqi, Liu Wei, Liu Zhichun. Experimental investigation on the start-up performance of a novel flat loop heat pipe with dual evaporators. Energy Rep 2022;8:7500–7. https://doi.org/10.1016/j.egyr.2022.05.248. ISSN 2352-4847.
[39] Weng Jingwen, Jossen Andreas, Stefanopoulou Anna, Ju Li, Feng Xuning, Offer Gregory. Fast-charging lithium-ion batteries require a systems engineering approach. Nat Energy 2025. https://doi.org/10.1038/s41560-025-01813-w. 10.1038/s41560-025-01813-w.
[40] Nemš Artur, Daniarta Sindu, Nemš Magdalena, Kolashiński Piotr, Ushak Svetlana. A review of artificial intelligence to thermal energy storage and heat transfer improvement in phase change materials. Sustain Mater Technol 2025;44:e01348. https://doi.org/10.1016/j.susmat.2025.e01348. ISSN 2214-9937. d oi: 10.1016/j.susmat.2025.e01348.
[41] Li Weiheng, Li Ao, Yuen Anthony Chun Yin, Chen Qian, Chen Timothy Bo Yuan, Cordeiro Ivan Miguel De Cachinho, Lin Peng. Optimisation of pcm passive cooling efficiency on lithium-ion batteries based on coupled cfd and ann techniques. Appl Therm Eng 2025;259:124874. https://doi.org/10.1016/j.applthermaleng.2024.124874. ISSN 1359-4311. do i: 10.1016/j.applthermaleng.2024.124874.
[42] Gu Xiaoyong, Lei Wenbo, Xi Jiacheng, Song Mengqiang. Structural optimization and battery temperature prediction of battery thermal management system based on machine learning. Case Stud Therm Eng 2024;62:105207. https://doi.org/10.1016/j.csite.2024.105207. ISSN 2214-157X. d oi: 10.1016/j.csite.2024.105207.
[43] Suwa Tohru. Prediction of latent heat storage transient thermal performance for integrated solar combined cycle using machine learning techniques. J Energy Storage 2024;76:109856. https://doi.org/10.1016/j.est.2023.109856. ISSN 2352-152X. d oi: 10.1016/j.est.2023.109856.
[44] Kiyak Burak, Oztop Hakan F, Ertam Fatih, Gokhan Aksoy I. An intelligent approach to investigate the effects of container orientation for pcm melting based on an xgboost regression model. Eng Anal Bound Elem 2024;161:202–13. https://doi.org/10.1016/j.enganabound.2024.01.018. ISSN 0955-7997. d o i: 10.1016/j.enganabound.2024.01.018.
[45] Bao Yuchen, Zhou Haojie, Li Ji. Physics-based machine learning optimization of thermoelectric assembly for maximizing waste heat recovery. Energy 2024;307:132821.
[46] Chang Shoujin, Liu Bing, Gao Xiaoying, Li Xuan, Meng Yingze, Hu Haitao. Numerical thermal analysis and structural optimization of cascaded pcm heat sinks for thermal management of electronics. Int J Heat Mass Tran 2025;236:126301. https://doi.org/10.1016/j.ijheatmasstransfer.2024.126301. ISSN 0017-9310. d o i: 10.1016/j.ijheatmasstransfer.2024.126301.
[47] Motahar Sadegh, Jahangiri Mehdi. Transient heat transfer analysis of a phase change material heat sink using experimental data and artificial neural network. Appl Therm Eng 2020;167:114817. https://doi.org/10.1016/j.applthermaleng.2019.114817. ISSN 1359-4311. d oi: 10.1016/j.applthermaleng.2019.114817.
[48] Zhang Ning, Zhang Zhiyuan, Li Jintao, Cao Xing. Performance analysis and prediction of hybrid battery thermal management system integrating pcm with air cooling based on machine learning algorithm. Appl Therm Eng 2024;257:124474. https://doi.org/10.1016/j.applthermaleng.2024.124474. ISSN 1359-4311. d oi: 10.1016/j.applthermaleng.2024.124474.
[49] Najafi Khaboshan Hasan, Jaliliantabar Farzad, Abdullah Abdul Adam, Pan chal Satyam, Azarinia Amiratabak. Parametric investigation of battery thermal man agement system with phase change material, metal foam, and fins; utilizing cfd and ann models. Appl Therm Eng 2024;247:123080. https://doi.org/10.1016/j.applthermaleng.2024.123080. ISSN 1359-4311. d oi: 10.1016/j.applthermaleng.2024.123080.
[50] Sridharan Srinivas, Srikanth R, Balaji C. Multi objective geometric optimization of phase change material based cylindrical heat sinks with internal stem and radial fins. Therm Sci Eng Prog 2018;5:238–51. https://doi.org/10.1016/j.tsep.2017.10.003. ISSN 2451-9049. d oi: 10. 1016/j.tsep.2017.10.003.
[51] Zhang Liwei, Shang Bichen, Sun Weijie, Tao Yao, Li Xueren, Tu Jiyuan. Data driven optimization of nano-pcm arrangements for battery thermal management based on lattice boltzmann simulation. Energy 2024;313:133670. https://doi.org/10.1016/j.energy.2024.133670. ISSN 0360-5442. d oi: 10. 1016/j.energy.2024.133670.
[52] Li Xueren, Zhang Liwei, Shang Bichen, Xiang Fang, Yao Tao, Ma Yin, Wang Yong, Tu Jiyuan. Thermal energy and thermo-economic analysis of pcm-tes for space heating based on low-temperature waste heat: an experimental and numerical study. Energy 2024;311:133286. https://doi.org/10.1016/j.energy.2024.133286. ISSN 0360-5442. d oi: 10.1016/j.energy.2024.133286.
[53] Zhang Bixiao, Zeng Zhuo, Yuan Nenglin, Shi Hong. Numerical investigation of lithium-ion battery thermal management system performance influenced by physical properties of pcm. J Energy Storage 2025;117:116141.
[54] Xie Shiwei, Xu Chengshan, Li Wei, Kang Yue, Feng Xuning, Wu Weixiong. Machine learning accelerated the performance analysis on pcm-liquid coupled battery thermal management system. J Energy Storage 2024;100:113479.
[55] Zhang Yingchun, Xie Gongnan, Karimipour Arash. Comprehensive analysis on the effect of asymmetric heat fluxes on microchannel slip flow and heat transfer via a lattice boltzmann method. Int Commun Heat Mass Tran 2020;118:104856. https://doi.org/10.1016/j.icheatmasstransfer.2020.104856. ISSN 0735-1933.
[56] Huo Yutao, Rao Zhonghao. The improved enthalpy-transforming based lattice boltzmann model for solid-liquid phase change. Int J Heat Mass Tran 2019;133:861–71. https://doi.org/10.1016/j.ijheatmasstransfer.2018.12.166. ISSN 0017-9310.
[57] Wang Zhengdao, Wei Yikun, Qian Yuehong. A simple direct heating thermal immersed boundary-lattice boltzmann method for its application in incompressible flow. Comput Math Appl 2020;80:1633–49. https://doi.org/10.1016/j.camwa.2020.08.003. ISSN 0898-1221.
[58] Arshad Adeel, Jabbal Mark, Yan Yuying. Preparation and characteristics evalua tion of mono and hybrid nano-enhanced phase change materials (nepcms) for thermal management of microelectronics. Energy Convers Manag 2020;205:112444. https://doi.org/10.1016/j.enconman.2019.112444. ISSN 0196-8904.
[59] Arıcı Müslüm, Tütüncü Ensar, Kan Miraç, Karabay Hasan. Melting of nanoparticle enhanced paraffin wax in a rectangular enclosure with partially active walls. Int J Heat Mass Tran 2017;104:7–17. https://doi.org/10.1016/j.ijheatmasstransfer.2016.08.017. ISSN 0017-9310.
[60] Humaira Tasnim Syeda, Hossain Rakib, Mahmud Shohel, Dutta Animesh. Con vection effect on the melting process of nano-pcm inside porous enclosure. Int J Heat Mass Tran 2015;85:206–20. https://doi.org/10.1016/j.ijheatmasstransfer.2015.01.073. ISSN 0017-9310.
[61] Al-Jethelah Manar SM, Humaira Tasnim Syeda, Mahmud Shohel, Dutta Animesh. Melting of nano-phase change material inside a porous enclosure. Int J Heat Mass Tran 2016;102:773–87. https://doi.org/10.1016/j.ijheatmasstransfer.2016.06.070. ISSN 0017-9310.
[62] Mencinger Jure. Numerical simulation of melting in two-dimensional cavity using adap tive grid. J Comput Phys 2004;198(1):243–64. https://doi.org/10.1016/j.jcp.2004.01.006. ISSN 0021-9991.
[63] Huo Yutao, Guo Yunqi, Rao Zhonghao. Investigation on the thermal performance of phase change material/porous medium-based battery thermal management in pore scale. Int J Energy Res 2019;43(2):767–78. https://doi.org/10.1002/er.4307. ISSN 0363-907X.
[64] Huo Yutao, Rao Zhonghao. Lattice boltzmann simulation for solid–liquid phase change phenomenon of phase change material under constant heat flux. Int J Heat Mass Tran 2015;86:197–206. https://doi.org/10.1016/j.ijheatmasstransfer.2015.03.006. ISSN 0017-9310. d oi: 10.1016/j.ijheatmasstransfer.2015.03.006.
[65] Hollmann Noah, Müller Samuel, Purucker Lennart, Krishnakumar Arjun, Körfer Max, Hoo Shi Bin, Schirrmeister Robin Tibor, Hutter Frank. Accurate predictions on small data with a tabular foundation model. Nature 2025;637(8045):319–26. https://doi.org/10.1038/s41586-024-08328-6. ISSN 1476-4687.
[66] Ekin Akÿurek, Schuurmans Dale, Jacob Andreas, Ma Tengyu, Zhou Denny. What learning algorithm is in-context learning? Investigations with linear models. arXiv preprint arXiv:221115661 2023. https://openreview.net/forum?id=0g0X4H8yN4.
[67] Garg Shivam, Tsipras Dimitris, Liang Percy S, Valiant Gregory. What can transformers learn in-context? A case study of simple function classes. Adv Neural Inf Process Syst 2022;35:30583–98.
[68] Müller Samuel, Hollmann Noah, Pineda Arango Sebastian, Grabocka Josif, Hutter Frank. Transformers can do bayesian inference. arXiv preprint arXiv:211210510 2022.
[69] Zhou Hattie, Bradley Arwen, Littwin Etai, Razin Noam, Saremi Omid, Susskind Josh, Bengio Samy, Nakkiran Preetum. What algorithms can transformers

learn? A study in length generalization. arXiv preprint arXiv:231016028 2024. https://openreview.net/forum?id=AssIuHnmHX.
[70] Li Xueren, Chen Ziqi, Yin Tang, Yihuan Yan, Shang Bichen, Shengjin Xu, Tu Jiyuan. An integrated cfd and machine learning analysis on pilots in-flight thermal comfort and productivity. Engineering Applications of Computational Fluid Mechanics 2024;18(1):2421002. https://doi.org/10.1080/19942060.2024.2421002. ISSN 1994-2060. d oi: 10.1080/19942060.2024.2421002.
[71] Chen Tianqi, Guestrin Carlos. Xgboost: a scalable tree boosting system. In: Proceedings of the 22nd acm sigkdd international conference on knowledge discovery and data mining; 2016. p. 785–94.
[72] Prokhorenkova Liudmila, Gusev Gleb, Vorobev Aleksandr, Dorogush Anna Veronika, Gulin Andrey. Catboost: unbiased boosting with categorical features. Adv Neural Inf Process Syst 2018;31.
[73] Li Xueren, Xu Ruipeng, Fan Jiaqi, Zhang Liwei, Sun Weijie, Kenjeres Sasa, Shang Yidan, Yang William. Evaluation of multi-output machine learning models for predicting inhaled particle deposition in the human upper and central airway. Powder Technol 2025;458:120924. ISSN 0032-5910.
[74] Scott M Lundberg, Su-In Lee. A unified approach to interpreting model predictions. Adv Neural Inf Process Syst 2017;30.
[75] Jilte Ravindra, Afzal Asif, Panchal Satyam. A novel battery thermal management system using nano-enhanced phase change materials. Energy 2021;219:119564. https://doi.org/10.1016/j.energy.2020.119564. ISSN 0360-5442. d oi: 10.1016/j.energy.2020.119564.
[76] Gu Xiaoyong, Lei Wenbo, Xi Jiacheng, Song Mengqiang. Structural optimization and battery temperature prediction of battery thermal management system based on machine learning. Case Stud Therm Eng 2024;62:105207.